arXiv:1411.6111v1 [astro-ph.HE] 22 Nov 2014

Searches for Anisotropies in the Arrival Directions of the Highest Energy Cosmic Rays Detected by the Pierre Auger Observatory

The Pierre Auger Collaboration

A. Aab[42], P. Abreu[64], M. Aglietta[53], E.J. Ahn[81], I. Al Samarai[29], I.F.M. Albuquerque[17], I. Allekotte[1], J. Allen[84], P. Allison[86], A. Almela[11, 8], J. Alvarez Castillo[57], J. Alvarez-Muñiz[74], R. Alves Batista[41], M. Ambrosio[44], A. Aminaei[58], L. Anchordoqui[80], S. Andringa[64], C. Aramo[44], V.M. Aranda [71], F. Arqueros[71], H. Asorey[1], P. Assis[64], J. Aublin[31], M. Ave[1], M. Avenier[32], G. Avila[10], N. Awal[84], A.M. Badescu[68], K.B. Barber[12], J. Bäuml[36], C. Baus[36], J.J. Beatty[86], K.H. Becker[35], J.A. Bellido[12], C. Berat[32], M.E. Bertaina[53], X. Bertou[1], P.L. Biermann[39], P. Billoir[31], S.G. Blaess[12], M. Blanco[31], C. Bleve[48], H. Blümer[36, 37], M. Boháčová[27], D. Boncioli[52], C. Bonifazi[23], R. Bonino[53], N. Borodai[62], J. Brack[78], I. Brancus[65], A. Bridgeman[37], P. Brogueira[64], W.C. Brown[79], P. Buchholz[42], A. Bueno[73], S. Buitink[58], M. Buscemi[44], K.S. Caballero-Mora[55 e], B. Caccianiga[43], L. Caccianiga[31], M. Candusso[45], L. Caramete[39], R. Caruso[46], A. Castellina[53], G. Cataldi[48], L. Cazon[64], R. Cester[47], A.G. Chavez[56], A. Chiavassa[53], J.A. Chinellato[18], J. Chudoba[27], M. Cilmo[44], R.W. Clay[12], G. Cocciolo[48], R. Colalillo[44], A. Coleman[87], L. Collica[43], M.R. Coluccia[48], R. Conceição[64], F. Contreras[9], M.J. Cooper[12], A. Cordier[30], S. Coutu[87], C.E. Covault[76], J. Cronin[88], A. Curutiu[39], R. Dallier[34, 33], B. Daniel[18], S. Dasso[5, 3], K. Daumiller[37], B.R. Dawson[12], R.M. de Almeida[24], M. De Domenico[46], S.J. de Jong[58, 60], J.R.T. de Mello Neto[23], I. De Mitri[48], J. de Oliveira[24], V. de Souza[16], L. del Peral[72], O. Deligny[29], H. Dembinski[37], N. Dhital[83], C. Di Giulio[45], A. Di Matteo[49], J.C. Diaz[83], M.L. Díaz Castro[18], F. Diogo[64], C. Dobrigkeit [18], W. Docters[59], J.C. D'Olivo[57], A. Dorofeev[78], Q. Dorosti Hasankiadeh[37], M.T. Dova[4], J. Ebr[27], R. Engel[37], M. Erdmann[40], M. Erfani[42], C.O. Escobar[81, 18], J. Espadanal[64], A. Etchegoyen[8, 11], P. Facal San Luis[88], H. Falcke[58, 61, 60], K. Fang[88], G. Farrar[84], A.C. Fauth[18], N. Fazzini[81], A.P. Ferguson[76], M. Fernandes[23], B. Fick[83], J.M. Figueira[8], A. Filevich[8], A. Filipčič[69, 70], B.D. Fox[89], O. Fratu[68], M.M. Freire[6], U. Fröhlich[42], B. Fuchs[36], T. Fujii[88], R. Gaior[31], B. García[7], D. Garcia-Gamez[30], D. Garcia-Pinto[71], G. Garilli[46], A. Gascon Bravo[73], F. Gate[34], H. Gemmeke[38], P.L. Ghia[31], U. Giaccari[23], M. Giammarchi[43], M. Giller[63], C. Glaser[40], H. Glass[81], M. Gómez Berisso[1], P.F. Gómez Vitale[10], P. Gonçalves[64], J.G. Gonzalez[36], N. González[8], B. Gookin[78], J. Gordon[86], A. Gorgi[53], P. Gorham[89], P. Gouffon[17], S. Grebe[58, 60], N. Griffith[86], A.F. Grillo[52], T.D. Grubb[12], F. Guarino[44], G.P. Guedes[19], M.R. Hampel[8], P. Hansen[4], D. Harari[1], T.A. Harrison[12], S. Hartmann[40], J.L. Harton[78], A. Haungs[37], T. Hebbeker[40], D. Heck[37], P. Heimann[42], A.E. Herve[37], G.C. Hill[12], C. Hojvat[81], N. Hollon[88], E. Holt[37], P. Homola[35], J.R. Hörandel[58, 60], P. Horvath[28], M. Hrabovský[28, 27], D. Huber[36], T. Huege[37], A. Insolia[46], P.G. Isar[66], I. Jandt[35], S. Jansen[58, 60], C. Jarne[4], M. Josebachuili[8], A. Kääpä[35], O. Kambeitz[36], K.H. Kampert[35], P. Kasper[81], I. Katkov[36], B. Kégl[30], B. Keilhauer[37], A. Keivani[87], E. Kemp[18], R.M. Kieckhafer[83], H.O. Klages[37], M. Kleifges[38], J. Kleinfeller[9], R. Krause[40], N. Krohm[35], O. Krömer[38], D. Kruppke-Hansen[35], D. Kuempel[40], N. Kunka[38], D. LaHurd[76], L. Latronico[53], R. Lauer[91], M. Lauscher[40], P. Lautridou[34], S. Le Coz[32], M.S.A.B. Leão[14], D. Lebrun[32], P. Lebrun[81], M.A. Leigui de Oliveira[22], A. Letessier-Selvon[31], I. Lhenry-Yvon[29], K. Link[36], R. López[54], K. Louedec[32], J. Lozano Bahilo[73], L. Lu[35, 75], A. Lucero[8], M. Ludwig[36], M. Malacari[12], S. Maldera[53], M. Mallamaci[43], J. Maller[34], D. Mandat[27], P. Mantsch[81], A.G. Mariazzi[4], V. Marin[34], I.C. Mariş[73], G. Marsella[48],

D. Martello[48], L. Martin[34, 33], H. Martinez[55], O. Martínez Bravo[54], D. Martraire[29], J.J. Masías Meza[3], H.J. Mathes[37], S. Mathys[35], J. Matthews[82], J.A.J. Matthews[91], G. Matthiae[45], D. Maurel[36], D. Maurizio[13], E. Mayotte[77], P.O. Mazur[81], C. Medina[77], G. Medina-Tanco[57], R. Meissner[40], M. Melissas[36], D. Melo[8], A. Menshikov[38], S. Messina[59], R. Meyhandan[89], S. Mićanović[25], M.I. Micheletti[6], L. Middendorf[40], I.A. Minaya[71], L. Miramonti[43], B. Mitrica[65], L. Molina-Bueno[73], S. Mollerach[1], M. Monasor[88], D. Monnier Ragaigne[30], F. Montanet[32], C. Morello[53], M. Mostafá[87], C.A. Moura[22], M.A. Muller[18, 21], G. Müller[40], S. Müller[37], M. Münchmeyer[31], R. Mussa[47], G. Navarra[53 ‡], S. Navas[73], P. Necesal[27], L. Nellen[57], A. Nelles[58, 60], J. Neuser[35], P.H. Nguyen[12], M. Niechciol[42], L. Niemietz[35], T. Niggemann[40], D. Nitz[83], D. Nosek[26], V. Novotny[26], L. Nožka[28], L. Ochilo[42], F. Oikonomou[87], A. Olinto[88], M. Oliveira[64], N. Pacheco[72], D. Pakk Selmi-Dei[18], M. Palatka[27], J. Pallotta[2], N. Palmieri[36], P. Papenbreer[35], G. Parente[74], A. Parra[54], T. Paul[80, 85], M. Pech[27], J. Pękala[62], R. Pelayo[54 d], I.M. Pepe[20], L. Perrone[48], E. Petermann[90], C. Peters[40], S. Petrera[49, 50], Y. Petrov[78], J. Phuntsok[87], R. Piegaia[3], T. Pierog[37], P. Pieroni[3], M. Pimenta[64], V. Pirronello[46], M. Platino[8], M. Plum[40], A. Porcelli[37], C. Porowski[62], R.R. Prado[16], P. Privitera[88], M. Prouza[27], V. Purrello[1], E.J. Quel[2], S. Querchfeld[35], S. Quinn[76], J. Rautenberg[35], O. Ravel[34], D. Ravignani[8], B. Revenu[34], J. Ridky[27], S. Riggi[46], M. Risse[42], P. Ristori[2], V. Rizi[49], W. Rodrigues de Carvalho[74], G. Rodriguez Fernandez[45], J. Rodriguez Rojo[9], M.D. Rodríguez-Frías[72], D. Rogozin[37], G. Ros[72], J. Rosado[71], T. Rossler[28], M. Roth[37], E. Roulet[1], A.C. Rovero[5], S.J. Saffi[12], A. Saftoiu[65], F. Salamida[29], H. Salazar[54], A. Saleh[70], F. Salesa Greus[87], G. Salina[45], F. Sánchez[8], P. Sanchez-Lucas[73], C.E. Santo[64], E. Santos[18], E.M. Santos[17], F. Sarazin[77], B. Sarkar[35], R. Sarmento[64], R. Sato[9], N. Scharf[40], V. Scherini[48], H. Schieler[37], P. Schiffer[41], D. Schmidt[37], O. Scholten[59 f], H. Schoorlemmer[89, 58, 60], P. Schovánek[27], A. Schulz[37], J. Schulz[58], J. Schumacher[40], S.J. Sciutto[4], A. Segreto[51], M. Settimo[31], A. Shadkam[82], R.C. Shellard[13], I. Sidelnik[1], G. Sigl[41], O. Sima[67], A. Śmiałkowski[63], R. Šmída[37], G.R. Snow[90], P. Sommers[87], J. Sorokin[12], R. Squartini[9], Y.N. Srivastava[85], S. Stanič[70], J. Stapleton[86], J. Stasielak[62], M. Stephan[40], A. Stutz[32], F. Suarez[8], T. Suomijärvi[29], A.D. Supanitsky[5], M.S. Sutherland[86], J. Swain[85], Z. Szadkowski[63], M. Szuba[37], O.A. Taborda[1], A. Tapia[8], A. Tepe[42], V.M. Theodoro[18], C. Timmermans[60, 58], C.J. Todero Peixoto[15], G. Toma[65], L. Tomankova[37], B. Tomé[64], A. Tonachini[47], G. Torralba Elipe[74], D. Torres Machado[23], P. Travnicek[27], E. Trovato[46], R. Ulrich[37], M. Unger[37, 84], M. Urban[40], J.F. Valdés Galicia[57], I. Valiño[74], L. Valore[44], G. van Aar[58], P. van Bodegom[12], A.M. van den Berg[59], S. van Velzen[58], A. van Vliet[41], E. Varela[54], B. Vargas Cárdenas[57], G. Varner[89], J.R. Vázquez[71], R.A. Vázquez[74], D. Veberič[30], V. Verzi[45], J. Vicha[27], M. Videla[8], L. Villaseñor[56], B. Vlcek[72], S. Vorobiov[70], H. Wahlberg[4], O. Wainberg[8, 11], D. Walz[40], A.A. Watson[75], M. Weber[38], K. Weidenhaupt[40], A. Weindl[37], F. Werner[36], A. Widom[85], L. Wiencke[77], B. Wilczyńska[62 ‡], H. Wilczyński[62], C. Williams[88], T. Winchen[35], D. Wittkowski[35], B. Wundheiler[8], S. Wykes[58], T. Yamamoto[88 a], T. Yapici[83], G. Yuan[82], A. Yushkov[42], B. Zamorano[73], E. Zas[74], D. Zavrtanik[70, 69], M. Zavrtanik[69, 70], A. Zepeda[55 b], J. Zhou[88], Y. Zhu[38], M. Zimbres Silva[18], M. Ziolkowski[42], F. Zuccarello[46]

[1] Centro Atómico Bariloche and Instituto Balseiro (CNEA-UNCuyo-CONICET), San Carlos de Bariloche, Argentina
[2] Centro de Investigaciones en Láseres y Aplicaciones, CITEDEF and CONICET, Argentina
[3] Departamento de Física, FCEyN, Universidad de Buenos Aires and CONICET, Argentina

[4] IFLP, Universidad Nacional de La Plata and CONICET, La Plata, Argentina

[5] Instituto de Astronomía y Física del Espacio (IAFE, CONICET-UBA), Buenos Aires, Argentina

[6] Instituto de Física de Rosario (IFIR) - CONICET/U.N.R. and Facultad de Ciencias Bioquímicas y Farmacéuticas U.N.R., Rosario, Argentina

[7] Instituto de Tecnologías en Detección y Astropartículas (CNEA, CONICET, UNSAM), and National Technological University, Faculty Mendoza (CONICET/CNEA), Mendoza, Argentina

[8] Instituto de Tecnologías en Detección y Astropartículas (CNEA, CONICET, UNSAM), Buenos Aires, Argentina

[9] Observatorio Pierre Auger, Malargüe, Argentina

[10] Observatorio Pierre Auger and Comisión Nacional de Energía Atómica, Malargüe, Argentina

[11] Universidad Tecnológica Nacional - Facultad Regional Buenos Aires, Buenos Aires, Argentina

[12] University of Adelaide, Adelaide, S.A., Australia

[13] Centro Brasileiro de Pesquisas Fisicas, Rio de Janeiro, RJ, Brazil

[14] Faculdade Independente do Nordeste, Vitória da Conquista, Brazil

[15] Universidade de São Paulo, Escola de Engenharia de Lorena, Lorena, SP, Brazil

[16] Universidade de São Paulo, Instituto de Física de São Carlos, São Carlos, SP, Brazil

[17] Universidade de São Paulo, Instituto de Física, São Paulo, SP, Brazil

[18] Universidade Estadual de Campinas, IFGW, Campinas, SP, Brazil

[19] Universidade Estadual de Feira de Santana, Brazil

[20] Universidade Federal da Bahia, Salvador, BA, Brazil

[21] Universidade Federal de Pelotas, Pelotas, RS, Brazil

[22] Universidade Federal do ABC, Santo André, SP, Brazil

[23] Universidade Federal do Rio de Janeiro, Instituto de Física, Rio de Janeiro, RJ, Brazil

[24] Universidade Federal Fluminense, EEIMVR, Volta Redonda, RJ, Brazil

[25] Rudjer Bošković Institute, 10000 Zagreb, Croatia

[26] Charles University, Faculty of Mathematics and Physics, Institute of Particle and Nuclear Physics, Prague, Czech Republic

[27] Institute of Physics of the Academy of Sciences of the Czech Republic, Prague, Czech Republic

[28] Palacky University, RCPTM, Olomouc, Czech Republic

[29] Institut de Physique Nucléaire d'Orsay (IPNO), Université Paris 11, CNRS-IN2P3, France

[30] Laboratoire de l'Accélérateur Linéaire (LAL), Université Paris 11, CNRS-IN2P3, France

[31] Laboratoire de Physique Nucléaire et de Hautes Energies (LPNHE), Universités Paris 6 et Paris 7, CNRS-IN2P3, Paris, France

[32] Laboratoire de Physique Subatomique et de Cosmologie (LPSC), Université Grenoble-Alpes, CNRS/IN2P3, France

[33] Station de Radioastronomie de Nançay, Observatoire de Paris, CNRS/INSU, France

[34] SUBATECH, École des Mines de Nantes, CNRS-IN2P3, Université de Nantes, France

[35] Bergische Universität Wuppertal, Wuppertal, Germany

[36] Karlsruhe Institute of Technology - Campus South - Institut für Experimentelle Kernphysik (IEKP), Karlsruhe, Germany

[37] Karlsruhe Institute of Technology - Campus North - Institut für Kernphysik, Karlsruhe, Germany

[38] Karlsruhe Institute of Technology - Campus North - Institut für Prozessdatenverarbeitung und Elektronik, Karlsruhe, Germany

[39] Max-Planck-Institut für Radioastronomie, Bonn, Germany

[40] RWTH Aachen University, III. Physikalisches Institut A, Aachen, Germany

[41] Universität Hamburg, Hamburg, Germany

[42] Universität Siegen, Siegen, Germany

[43] Università di Milano and Sezione INFN, Milan, Italy

[44] Università di Napoli "Federico II" and Sezione INFN, Napoli, Italy

[45] Università di Roma II "Tor Vergata" and Sezione INFN, Roma, Italy

[46] Università di Catania and Sezione INFN, Catania, Italy

[47] Università di Torino and Sezione INFN, Torino, Italy

[48] Dipartimento di Matematica e Fisica "E. De Giorgi" dell'Università del Salento and Sezione INFN, Lecce, Italy

[49] Dipartimento di Scienze Fisiche e Chimiche dell'Università dell'Aquila and INFN, Italy

[50] Gran Sasso Science Institute (INFN), L'Aquila, Italy

[51] Istituto di Astrofisica Spaziale e Fisica Cosmica di Palermo (INAF), Palermo, Italy

[52] INFN, Laboratori Nazionali del Gran Sasso, Assergi (L'Aquila), Italy

[53] Osservatorio Astrofisico di Torino (INAF), Università di Torino and Sezione INFN, Torino, Italy

[54] Benemérita Universidad Autónoma de Puebla, Puebla, Mexico

[55] Centro de Investigación y de Estudios Avanzados del IPN (CINVESTAV), México, Mexico

[56] Universidad Michoacana de San Nicolas de Hidalgo, Morelia, Michoacan, Mexico

[57] Universidad Nacional Autonoma de Mexico, Mexico, D.F., Mexico

[58] IMAPP, Radboud University Nijmegen, Netherlands

[59] KVI - Center for Advanced Radiation Technology, University of Groningen, Netherlands

[60] Nikhef, Science Park, Amsterdam, Netherlands

[61] ASTRON, Dwingeloo, Netherlands

[62] Institute of Nuclear Physics PAN, Krakow, Poland

[63] University of Łódź, Łódź, Poland

[64] Laboratório de Instrumentação e Física Experimental de Partículas - LIP and Instituto Superior Técnico - IST, Universidade de Lisboa - UL, Portugal

[65] 'Horia Hulubei' National Institute for Physics and Nuclear Engineering, Bucharest- Magurele, Romania

[66] Institute of Space Sciences, Bucharest, Romania

[67] University of Bucharest, Physics Department, Romania

[68] University Politehnica of Bucharest, Romania

[69] Experimental Particle Physics Department, J. Stefan Institute, Ljubljana, Slovenia

[70] Laboratory for Astroparticle Physics, University of Nova Gorica, Slovenia

[71] Universidad Complutense de Madrid, Madrid, Spain

[72] Universidad de Alcalá, Alcalá de Henares (Madrid), Spain

[73] Universidad de Granada and C.A.F.P.E., Granada, Spain

[74] Universidad de Santiago de Compostela, Spain

[75] School of Physics and Astronomy, University of Leeds, United Kingdom

[76] Case Western Reserve University, Cleveland, OH, USA

[77] Colorado School of Mines, Golden, CO, USA

[78] Colorado State University, Fort Collins, CO, USA

[79] Colorado State University, Pueblo, CO, USA

[80] Department of Physics and Astronomy, Lehman College, City University of New York, New

York, USA

[81] Fermilab, Batavia, IL, USA

[82] Louisiana State University, Baton Rouge, LA, USA

[83] Michigan Technological University, Houghton, MI, USA

[84] New York University, New York, NY, USA

[85] Northeastern University, Boston, MA, USA

[86] Ohio State University, Columbus, OH, USA

[87] Pennsylvania State University, University Park, PA, USA

[88] University of Chicago, Enrico Fermi Institute, Chicago, IL, USA

[89] University of Hawaii, Honolulu, HI, USA

[90] University of Nebraska, Lincoln, NE, USA

[91] University of New Mexico, Albuquerque, NM, USA

(‡) Deceased

(a) Now at Konan University

(b) Also at the Universidad Autonoma de Chiapas on leave of absence from Cinvestav

(d) Now at Unidad Profesional Interdisciplinaria de Ingeniería y Tecnologías Avanzadas del IPN, México, D.F., México

(e) Now at Universidad Autónoma de Chiapas, Tuxtla Gutiérrez, Chiapas, México

(f) Also at Vrije Universiteit Brussels, Belgium

ABSTRACT

We analyze the distribution of arrival directions of ultra-high energy cosmic rays recorded at the Pierre Auger Observatory in 10 years of operation. The data set, about three times larger than that used in earlier studies, includes arrival directions with zenith angles up to 80°, thus covering from $-90°$ to $+45°$ in declination. After updating the fraction of events correlating with the active galactic nuclei (AGNs) in the Véron-Cetty and Véron catalog, we subject the arrival directions of the data with energies in excess of 40 EeV to different tests for anisotropy. We search for localized excess fluxes and for self-clustering of event directions at angular scales up to 30° and for different threshold energies between 40 EeV and 80 EeV. We then look for correlations of cosmic rays with celestial structures both in the Galaxy (the Galactic Center and Galactic Plane) and in the local Universe (the Super-Galactic Plane). We also examine their correlation with different populations of nearby extragalactic objects: galaxies in the 2MRS catalog, AGNs detected by Swift-BAT, radio galaxies with jets and the Centaurus A galaxy. None of the tests shows a statistically significant evidence of anisotropy. The strongest departures from isotropy (post-trial probability $\sim$1.4%) are obtained for cosmic rays with $E > 58$ EeV in rather large windows around Swift AGNs closer than 130 Mpc and brighter than 10^{44} erg/s (18° radius) and around the direction of Centaurus A (15° radius).

1. Introduction

The measurements of the energy spectrum of ultra-high energy cosmic rays (UHE-CRs), their mass composition and the celestial distribution of their arrival directions serve in a complementary way to understand their origin. The acceleration mechanism as well as the propagation in the Galactic and intergalactic media can be constrained by detailed studies of spectral features and of the evolution of the mass composition as a function of energy. In turn, and despite the fact that UHECRs are mostly charged particles, information on the sources might be contained in the distribution of their arrival directions, especially above a few tens of EeV where the magnetic deflections (at least of those cosmic rays with a small charge) may be of only a few degrees. A number of facts contribute to this expectation. Stringent limits to the flux of primary photons at such energies (Abraham et al. 2009) strongly constrain top-down models for the origin of UHECRs and hence favor astrophysical objects as accelerators. Also, at such energies the flux of cosmic rays is expected to be suppressed due to energy losses in their interactions with photons of the Cosmic Microwave Background (CMB) by the so-called GZK (Greisen-Zatsepin-Kuz'min) effect (Greisen 1966; Zatsepin & Kuzmin 1966). These interactions limit the distance from which a source can contribute to the flux at Earth. For instance, this distance has to be less than ~ 200 Mpc for protons or Fe nuclei with energies above 60 EeV, and even smaller for intermediate mass nuclei (Harari et al. 2006). Thus, the number of candidate sources which could contribute to the measured fluxes at the highest energies is significantly reduced. Finally, the arrival directions of UHECRs are not expected to be completely isotropized by magnetic fields due to their very high rigidity.

A suppression in the flux of UHECRs at energies above 40 EeV has been established experimentally beyond any doubt (Abbasi et al. 2008; Abraham et al. 2008b; Abu-Zayyad et al. 2013). The energy at which the spectrum steepens is in accordance with that expected from the GZK effect. However, this alone does not allow one to conclude whether the observed feature is due to propagation effects or to source properties, i.e., the maximum energy achievable in the acceleration process. Information on the nature of UHECRs is one of the keys in discriminating between the two scenarios. The measurement of the cosmic ray composition has been addressed through the measurement of the depth of shower maximum, X_{max} (Abraham et al. 2010a; Aab et al. 2014; Abbasi et al. 2010, 2014b). Interpretations of Auger data through the most updated models of hadronic interactions (Abreu et al. 2013b; Aab et al. 2014) indicate that the fraction of heavy nuclei increases above the energy of the ankle (the spectral hardening taking place at $E \simeq 5$ EeV) and up to the highest energies. However, the small number of events does not allow one to probe the primary mass evolution in detail at energies in excess of 40 EeV, where there have been only 18 events available for the composition analysis.

To complement the spectrum and mass measurements, several studies of the distribu-

tion of arrival directions have been made with UHECR data. Using an early data set the Pierre Auger Collaboration reported evidence of anisotropy with a confidence level of 99% in the distribution of cosmic rays with energy above about 57 EeV (Abraham et al. 2007, 2008a). That analysis was based on the finding, through an *a-priori* test, of a correlation within a small angular separation (3.1°) between the UHECR arrival directions and the locations of nearby active galaxies (within 75 Mpc) in the Véron-Cetty and Véron (VCV) catalog (Veron-Cetty & Veron 2006). With an enlarged data set the correlating fraction was found in later analyses to be lower (Abreu et al. 2010; Kampert et al. 2012), although still ∼3σ above expectations from an isotropic distribution. Other tests on the data, using a variety of astronomical catalogs, yielded some further hints but no significant evidence of anisotropy (Abreu et al. 2010). It is interesting to note that both the Pierre Auger and the Telescope Array Collaborations have reported, although with a limited significance, concentrations of very high energy events in regions of the sky of ∼20° radius, namely for 18° around the radio galaxy Centaurus A (Cen A) in the case of Auger (Abreu et al. 2010) and in a 20° radius window at declination $\delta = 43°$ in the case of the Telescope Array (Abbasi et al. 2014a). Note that the hot spot observed around Cen A is outside the field of view of the Telescope Array, while the one observed by the Telescope Array is only partially inside the field of view of the Auger Observatory when highly-inclined events are considered.

In the present situation where the origin of the suppression in the flux of the UHE-CRs has not yet been understood, their mass composition is not precisely known and the predictions of their deflections in magnetic fields are uncertain (also due to uncertainties in models of magnetic fields, see for example Farrar (2014) for a recent review), a large number of events is essential in looking for anisotropies in a sky map. Whatever the origin of the suppression in their flux and whatever their nature, UHECRs are still expected to come from sources relatively close to the Earth where the galaxies are distributed non uniformly. Even if low-charge particles were to contribute only a fraction of the primary cosmic rays, anisotropic signals on small angular scales may show up as the number of events gathered increases. In turn, should the UHECRs be significantly deflected, either due to their large charge or due to the presence of strong intervening magnetic fields, directional excesses might still be found at larger angular scales. Searches for such anisotropies have been made so far with data sets including a few dozen cosmic rays (for instance in Abreu et al. (2010) we published the arrival directions and energies of 69 events above 55 EeV and zenith angle $\theta \leq 60°$, corresponding to an exposure of 20,370 km^2 sr yr). In this paper we present a study of the arrival directions of UHECRs detected by the Pierre Auger Observatory in more than 10 years of data taking, with an exposure of about 66,000 km^2 sr yr. The data set, including more than 600 events above 40 EeV, is described in Section 2. By including for the first time cosmic rays with zenith angles up to 80°, the field of view of the Auger Observatory has been extended to cover

from $-90°$ to $+45°$ in declination.

In the later sections we analyze the distribution of the arrival directions. In Section 3 we update the fraction of events correlating with AGNs in the VCV catalog. In spite of the large data set (three times larger than that used in Abreu et al. (2010)), this test does not substantiate the initial evidence of anisotropy at energies larger than 53 EeV[1]. We consequently explore in the later sections the set of arrival directions for cosmic rays observed with energies above 40 EeV. Since this energy corresponds to the onset of the suppression in the observed flux, we expect a limited number of contributing sources above such a threshold. Also, above this energy the angular deflections caused by intervening magnetic fields are expected to be of the order of a few degrees for protons, and Z times larger in the case of nuclei with atomic number Z. We perform various tests to search for anisotropies in the data set, exploring a wide range of angular windows between $1°$ and $30°$ and energy thresholds from 40 EeV up to 80 EeV. The angular range is motivated, at the lower end, by the angular resolution of the measurement of the arrival directions and, at the higher end, by the large deflections expected if cosmic rays are high-Z nuclei. Considering energy thresholds higher than 40 EeV may help because it may involve smaller deflections and smaller GZK horizons, with the upper value of 80 EeV still allowing to have a sizeable number of events (22) in the analysis. In Section 4 we study "intrinsic" anisotropies as can be revealed by the search for localized excesses of events over the exposed sky and by the analysis of the autocorrelation of arrival directions. In Section 5 we search for correlations with known astrophysical structures, such as the Galactic and Super-Galactic Planes and the Galactic Center. We study the cross-correlation with astrophysical objects that could be considered as plausible candidates for UHECR sources in Section 6. Specifically, we exploit flux-limited catalogs of galaxies (2MRS), of AGNs observed in X-rays (Swift BAT-70) and of radio galaxies with jets. For the last two samples, we perform an additional study, considering different thresholds in the AGN intrinsic luminosity. Finally, in Section 7 we focus on the distribution of events around the direction of Centaurus A. After summarizing the main results in Section 8 we report in the Appendix the list of arrival directions and energies of the 231 UHECRs with energies above 52 EeV detected by the Pierre Auger Observatory between 2004 January 1 and 2014 March 31[2].

---

[1]This threshold was 57 EeV in the original calibration used in Abraham et al. (2007, 2008a). It became 55 EeV with the updated reconstruction used in Abreu et al. (2010), corresponding to approximately 53 EeV in the new energy scale considered in the present work (see Section 2).

[2]The list of the events is available also at `http://www.auger.org/data/AugerUHECR2014.txt`.

2. The Data Set

The Pierre Auger Observatory (Abraham et al. 2004) is located in Malargüe, Argentina, at latitude 35.2° S, longitude 69.5° W and an average altitude of 1400 m a.s.l. It comprises a surface detector (SD) made up of an array of water-Cherenkov stations overlooked by an air-fluorescence detector (FD) comprising a total of 27 telescopes at four sites on the perimeter of the array. The array consists of 1660 water-Cherenkov stations covering an area of about 3000 km^2. The SD samples the particle components of extensive air showers (mainly muons, electrons, and photons) with a duty cycle of nearly 100%.

The data set analyzed here includes cosmic rays with energy above 40 EeV recorded by the SD from 2004 January 1 up to 2014 March 31. In earlier analyses of the arrival directions we have used events with zenith angles less than 60° (referred to as *vertical*). Here we include, for the first time, those with zenith angles from 60° up to 80° (dubbed *inclined*). Selection, reconstruction and energy determination are different for the two event sets. The main characteristics of the data sets, including energy and angular resolution, are outlined below and details can be found in Ave M. et al. (2007); Aab et al. (2014).

Vertical events are accepted if at least four of the closest stations to the one with the highest signal are operational at the time of the event. We also require that the reconstructed shower core be contained within a triangle of operational stations, either equilateral or isosceles, of contiguous stations. This event selection, a less stringent one than that used in earlier works (where five operational neighboring stations were required), has been carefully studied using data. It ensures an accurate event reconstruction given the large multiplicity of triggered detectors (on average more than 14 stations are triggered in events with energy above 40 EeV). It also allows us to increase the number of vertical events by about 14% in the period considered. On the other hand, for inclined events we require that at least five active stations surround the station closest to the core position. Given the large footprint of inclined showers on the ground (the average station multiplicity is larger than 30), such a fiducial criterion guarantees adequate containment inside the array. The described selections lead to 454 vertical and 148 inclined events with $E \geq 40$ EeV.

The trigger and selection efficiency is 100% for energies above 3 (4) EeV for vertical (inclined) showers. The exposure is consequently determined by purely geometrical considerations (Abraham et al. 2010b; Aab et al. 2013) in both cases and for the period considered here it amounts to 51,753 km^2 sr yr and 14,699 km^2 sr yr, for the vertical and inclined samples, respectively.

For both data sets the arrival directions of cosmic rays are determined from the relative arrival times of the shower front in the triggered stations. The angular resolution, defined as the radius around the true cosmic ray direction that would contain 68% of the reconstructed shower directions, is better than 0.9° for energies above 10 EeV (Bonifazi et al.

2009).

The ground parameters used to estimate the primary energy are different for the two data sets. The estimator for the primary energy of vertical showers is the reconstructed signal at 1000 m from the shower axis, denoted $S(1000)$. The energy reconstruction of an inclined shower is based on the muon content, denoted N_{19}, relative to a simulated proton shower with energy 10^{19} eV. In both cases, the energy estimators are calibrated using hybrid events (detected simultaneously by SD and FD) and using the quasi-calorimetric energy determination obtained with the air fluorescence detector (Aab et al. 2013, 2014). The statistical uncertainty in the energy determination is smaller than 12% for energies above 10 EeV (Aab et al. 2014; Abreu et al. 2011). The systematic uncertainty in the absolute energy scale, common to the two data sets, is 14%. The Pierre Auger Collaboration has updated the energy scale in Verzi et al. (2013) accounting for recent measurements of the fluorescence yield (Ave et al. 2013), a better estimate of the invisible energy (Tueros et al. 2013), a deeper understanding of the detector, and an improved event reconstruction. The energy threshold of 55 EeV used in our previous publication (Abreu et al. 2010) corresponds now to approximately 53 EeV with the new energy scale.

We note that the relative number of vertical and inclined events above 40 EeV, $454/148 \simeq 3.07 \pm 0.29$, is consistent in view of the Poissonian fluctuations with the corresponding ratio of exposures, $51,753/14,699 \simeq 3.52$. On the other hand, the 14% difference between these ratios could also result from a $\sim$4% mismatch between the vertical and inclined energy calibrations, which is compatible with the uncorrelated systematic uncertainties on the energy scale.

3.   Note on the Anisotropy Test with the VCV Catalog

One of the anisotropy tests performed in our previous works was based on the Véron-Cetty and Véron catalog of active galactic nuclei (Veron-Cetty & Veron 2006). In an initial study we considered vertical events with $E \geq 40$ EeV collected from 2004 January 1 to 2006 May 26 (Period I). We performed an exploratory scan over the energy threshold of the events, their angular separation from AGNs and the maximum AGN redshift. We found that the most significant excess appeared in the correlation of events with energy above 57 EeV and lying within 3.1° of those AGNs closer than 75 Mpc. These parameters were then used for a search on independent data where it was found that 8 out of 13 events correlated, while 2.7 events (i.e., 21% of the total) were expected to correlate by chance for an isotropic distribution of arrival directions. This finding had a probability of 1.7×10^{-3} of happening by chance (Abraham et al. 2007, 2008a). Subsequent analyses with enlarged statistics yielded a correlation still above isotropic expectations but with a smaller strength and essentially dominated by the initial excess. The level of correlation

was $(38^{+7}_{-6})\%$ in Abreu et al. (2010) and $(33 \pm 5)\%$ in Kampert et al. (2012).

Here we update this analysis, for historical reasons, by using the vertical data set described in Section 2 and the VCV catalogue used in Abraham et al. (2007). Excluding Period I, there are 146 events above 53 EeV: 41 events correlate with VCV AGNs, with the angular and distance parameters fixed by the exploratory scan. The updated fraction of correlations is then $(28.1^{+3.8}_{-3.6})\%$, which is 2 standard deviations above the isotropic expectation of 21%. On the other hand, note that since the VCV correlations involve many different regions of the sky (besides the fact that CRs with different energies have significant time delays), an explanation of the reduced correlation found after 2007 in terms of a transient nature of the signal would not be natural. Hence, the high level of correlation found initially was probably affected by a statistical fluctuation. We conclude that this particular test does not yield a significant indication of anisotropy with the present data set.

4. General Anisotropy Tests

4.1. Search for a Localized Excess Flux over the Exposed Sky

A direct analysis of cosmic ray arrival directions is the blind search for excesses of events over the visible sky. To this aim we sample the exposed sky using circular windows with radii varying from $1°$ up to $30°$, in $1°$ steps. The centers of the windows are taken on a $1° \times 1°$ grid. The energy threshold of the events used to build the maps is varied from 40 EeV up to 80 EeV in steps of 1 EeV. To detect an excess we compare, for every window and energy threshold, the number of observed events, n_{obs}, with that expected from an isotropic flux of cosmic rays, n_{exp}. The expected number of events for an isotropic distribution is obtained, for each sky direction, by numerically integrating the geometric exposures in the corresponding windows[3].

For each window we calculate the binomial probability p of observing by chance in an isotropic flux an equal to, or larger number of events than that found in the data. We find the minimum probability, $p = 5.9 \times 10^{-6}$, at an energy threshold of 54 EeV and in a $12°$-radius window centered at right ascension and declination $(\alpha, \delta) = (198°, -25°)$, i.e., for Galactic longitude and latitude $(\ell, b) = (-51.1°, 37.6°)$, for which $n_{obs}/n_{exp} = 14/3.23$. The map of the Li-Ma (Li & Ma 1983) significances of the excesses of events with $E \geq 54$ EeV in windows of $12°$ radius is shown in Figure 1. The highest significance region just discussed, having a Li-Ma significance of 4.3σ, is indicated with a black circle. It is close

---

[3]We use the total number of vertical and inclined events to estimate the relative exposures of the two samples. Since the triggering is different in the two cases, this fraction is non-trivial.

to the Super-Galactic Plane, indicated with a dashed line, and not far from the direction of Centaurus A, indicated with a white star. One should keep in mind that although the effects of a turbulent magnetic field would be just to spread a signal around the direction towards the source, a regular field coherent over large scales would give rise to a shift of the excess in a direction orthogonal to that of the magnetic field, being the size of both effects energy dependent.
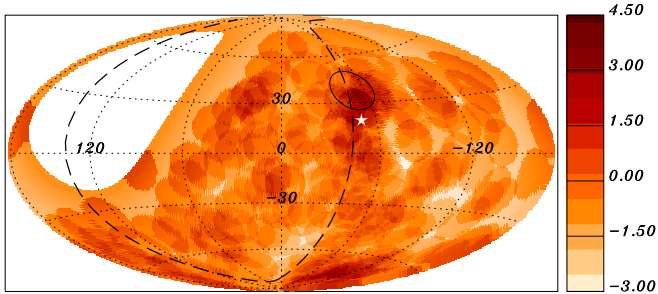

Fig. 1.— Map in Galactic coordinates of the Li-Ma significances of overdensities in 12°-radius windows for the events with $E \geq 54$ EeV. Also indicated are the Super-Galactic Plane (dashed line) and Centaurus A (white star).

To assess the significance of this excess we simulated 10,000 sets of isotropic arrival directions containing the same number of events as the data set. In doing so, we keep the original energies of the events and assign to them random arrival directions according to the geometric exposure, choosing randomly between vertical and inclined events according to their relative exposures. We apply to the simulated sets the same scans in angle and energy as those applied to the data. We find that values smaller than $p = 5.9 \times 10^{-6}$ are obtained in 69% of isotropic simulations and hence the excess found in the data turns out to be compatible with the maximum excesses expected in isotropic simulations. We note that in the region of the hot-spot reported by the Telescope Array Collaboration (Abbasi et al. 2014a), a 20° radius circular window centered at $(\alpha, \delta) = (146.7°, 43.2°)$, which is partially outside our field of view, we expect to see 0.97 events with $E > 53$ EeV if the distribution were isotropic and 1 event is observed.

4.2. The Autocorrelation of Events

Another simple way to test the clustering of arrival directions is through an autocorrelation analysis, which is particularly useful when several sources lead to excesses around them on a similar angular scale. With this method one looks for excesses in the number of

pairs of events, i.e., excesses of "self-clustering," namely, we count the number of pairs of events, $N_{\mathrm{p}}(\psi, E_{\mathrm{th}})$, above a given energy threshold E_{th} that are within a certain angular distance ψ. We do this at different energy thresholds, from 40 EeV up to 80 EeV (in steps of 1 EeV) and we look at angular scales from $1°$ up to $30°$ (in steps of $0.25°$ up to $5°$, and of $1°$ for larger angles). To identify an excess we compare the observed number of pairs with that expected from an isotropic distribution having the same number of arrival directions above the corresponding energy threshold. For each energy threshold and angle we then calculate the fraction of isotropic simulations having an equal number to, or more pairs than the data, $f(\psi, E_{\mathrm{th}})$.
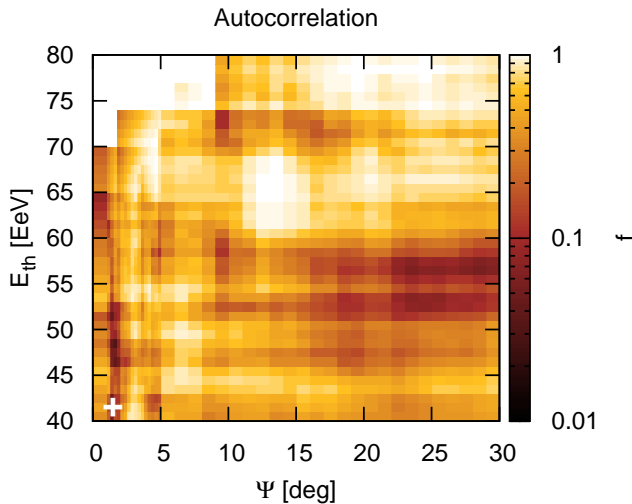

Fig. 2.— Fraction f obtained in the autocorrelation of events versus ψ and E_{th}.

The result is shown in Figure 2 as a function of the angular distance and the energy threshold. The color code indicates the values obtained for f. The white cross corresponds to the parameter values leading to the minimum value of this fraction, $f_{\min} = 0.027$, which happens for $\psi = 1.5°$ and $E_{\mathrm{th}} = 42$ EeV. For these parameters, 30 pairs are expected on average for isotropic simulations while 41 are observed in the data. We calculate the post-trial probability for this excess, P, as the fraction of isotropic simulations which under a similar scan over E_{th} and ψ lead to a value of $f_{\min}$ smaller than the one obtained with the data. The resulting value, $P \simeq 70\%$, indicates that the autocorrelation is compatible with the expectations from an isotropic distribution of arrival directions.
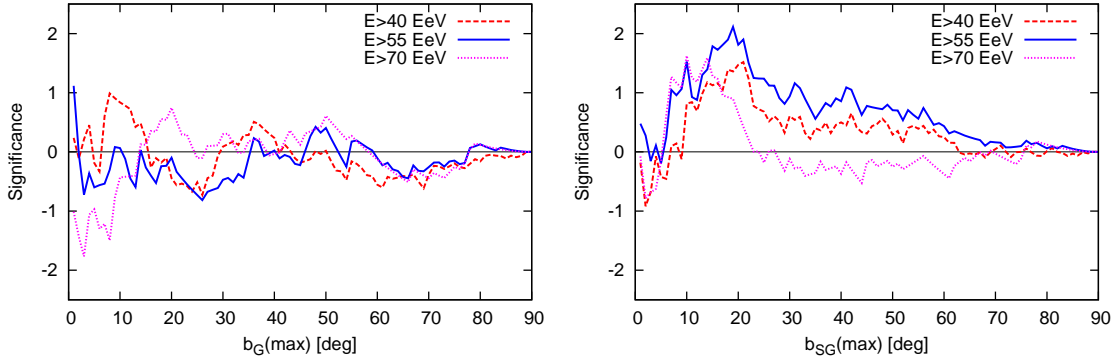
Fig. 3.— The significance as a function of Galactic (left) or Super-Galactic (right) latitude band half width, for events with energies above 40, 55 or 70 EeV.
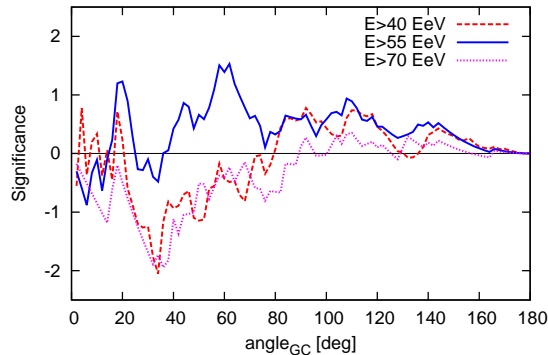

Fig. 4.— Significance of overdensities in circular windows around the Galactic Center as a function of the angular radius of the window, for events with energies above 40, 55 or 70 EeV.

5. Search for Correlations with the Galaxy and with the Super-Galactic Plane

In the previous section we tested the intrinsic distribution of arrival directions of UHECRs, i.e., without formulating any hypothesis on the distribution of their sources. In the following we consider specific astrophysical structures and objects as candidate sources. In this section we search for correlations with the Galactic and the Super-Galactic Planes as well as with the Galactic Center. On the one hand, a Galactic origin of UHECRs might give rise to an excess of arrival directions near the plane of the Galaxy, especially if a low-Z primary component contributes to the CR flux. On the other hand, nearby galaxies (within 100 Mpc) show a clustering along the so-called Super-Galactic Plane, which contains several prominent (super) clusters such as Virgo, Centaurus, Norma, Pavo-Indus, Perseus-Pisces, Coma, etc., and hence extragalactic cosmic rays could be clustered near the Super-Galactic Plane.

We search for excesses of events as a function of Galactic (Super-Galactic) latitude, $b_{\rm G}$ ($b_{\rm SG}$), considering different latitude bands, $|b| < b({\rm max})$, with $b({\rm max})$ indicating the half width of the band. To identify an excess we compare the number of observed events, $n_{\rm obs}$, to that expected from an isotropic distribution of arrival directions, $n_{\rm exp}$, obtained as the average over isotropic simulations of the number of events within the latitude band considered. The significance of an excess is taken as $\sigma \equiv (n_{\rm obs} - n_{\rm exp})/\sqrt{n_{\rm exp}}$. The results are shown in Figure 3 as a function of $b({\rm max})$. We show the results for events with energies above three illustrative thresholds, 40 EeV, 55 EeV and 70 EeV, respectively. The left (right) panel shows the significance as a function of Galactic (Super-Galactic) latitude band half width. No significant excess is observed in any latitude band from either of the two planes, although a slight excess is apparent within $\sim 20°$ of the Super-Galactic Plane for the three energy bins considered.

The overdensities in circular windows around the Galactic Center are shown in Figure 4 as a function of the angular radius. Again no significant excess results for any of the windows and energy thresholds considered.

6.   Search for Cross-Correlations with Astrophysical Catalogs

In this section we search for correlations of the set of arrival directions with the celestial distribution of potential nearby cosmic ray sources. We choose approximately uniform and complete catalogs, namely the 2MRS catalog of galaxies (Huchra et al. 2012), the Swift-BAT (Baumgartner et al. 2013) X-ray catalog of AGNs[4] and a catalog of radio galaxies with jets recently compiled in Van Velzen et al. (2012). The three samples are quite complementary in identifying possible cosmic ray sources. The normal galaxies that dominate the 2MRS catalog may trace the locations of gamma ray bursts and/or fast spinning newborn pulsars, whereas X-rays observed by Swift identify AGNs hosted mainly by spiral galaxies, and the radio emission catalog selects extended jets and radio lobes of AGNs hosted mainly by elliptical galaxies.

The 2MASS Redshift Survey (2MRS) (Huchra et al. 2012) maps the distribution of galaxies in the nearby universe. It covers 91% of the sky, except for Galactic latitudes $|b| < 5°$ (and $|b| < 8°$ for longitudes within $30°$ of the Galactic Center). In the region covered it is essentially complete (at 97.6%) for magnitudes brighter than $K_s = 11.75$. It contains 43,533 galaxies with measured redshift[5]: 37,209 of them are within 200 Mpc and

---

[4]The 2MRS and Swift catalogs have been updated after our earlier study of correlations in Abreu et al. (2010); Kampert et al. (2012).

[5]We adopt hereafter a Hubble constant of $H_0 = 70$ km/s/Mpc and the effective distances considered are taken as $D \equiv zc/H_0$, with z the source redshift obtained from the catalog.

16,422 within 100 Mpc. About 90% of its objects have a redshift $z < 0.05$, which is the range of distances of interest for UHECR correlation studies due to the effects of the GZK horizon.

The Swift-BAT 70-month X-ray catalog (Baumgartner et al. 2013) includes sources detected in 70 months of observation of the BAT hard X-ray detector on the Swift gamma-ray burst observatory. It contains a total of 1210 objects: 705 of them are AGN-like (Seyfert I and II, other AGNs, blazars and QSOs) with measured redshift. The catalog is complete over 90% of the sky for fluxes $> 13.4 \times 10^{-12}$ erg/(s cm^2), measured in the X-ray band from 14 to 195 keV. We use this cut in flux hereafter to have a more uniform sample of nearby AGNs. 489 AGN-like objects survive the cut: 296 of them are within 200 Mpc and 160 are within 100 Mpc.

The third catalog we use is a compilation of radio galaxies produced in Van Velzen et al. (2012). This is a combination of catalogs of observations at 1.4 GHz (NRAO VLA Sky Survey (Condon et al. 1998)) and 843 MHz (Sydney University Molonglo Sky Survey (Mauch et al. 2003)), with redshifts of associated objects taken from 2MRS. A flux limit of 213 mJy (289 mJy) at 1.4 GHz (843 MHz) is imposed to the objects from each respective catalog, which would correspond to the flux of Cen A as seen from a distance of about 200 Mpc. We select from this catalog the radio galaxies having jets, which constitute a set of attractive candidates for UHECR sources. There are in total 407 such jetted radio galaxies: 205 are within 200 Mpc and 56 are within 100 Mpc (for this catalog we compute the distance using the redshift corrected for peculiar velocities that are also provided). We note that the majority of these radio galaxies are different from the Swift-BAT AGNs detected in X-rays. It is also important to keep in mind that although we analyze each catalog individually, it is possible that different types of sources (i.e., from different catalogs) might be contributing to the overall UHECR fluxes.

Below we first study the cross-correlation with the three complete flux-limited catalogs (with the flux limits just described), including objects up to different maximum distances. This selection is based on the apparent luminosity, and is motivated by the fact that nearby sources may contribute significantly to the fluxes (in their corresponding electromagnetic band as well as in CRs) even if they are intrinsically fainter than far away sources. In the case of the AGNs in the Swift and radio-galaxy catalogs we also scan on the measured intrinsic luminosity of the objects. This is motivated by the fact that the maximum CR energy E_{max} achievable at the sources may be linked to the intrinsic electromagnetic bolometric luminosity $\mathcal{L}$ of the source. In particular one could expect that $(E_{max}/Z)^2 \propto \mathcal{L}$ if the energy density in the magnetic field is in equipartition with the energy in synchrotron emitting electrons in the acceleration region (see, e.g., Farrar & Gruzinov (2009)). Hence, it might happen that only sources intrinsically brighter than some given luminosity are able to accelerate CRs above the threshold energies considered in this paper. On the other

hand, for the radio galaxies the luminosity is also correlated with the Fanaroff-Riley class, with FRII galaxies being generally brighter than FRI ones.

6.1. Cross-Correlation with Flux-Limited Samples

The basis of the cross-correlation technique is a counting of the number of pairs between UHE events and objects in the chosen catalogs. In a similar way to the analyses described in previous sections, we scan over energy threshold ($40\ \mathrm{EeV} \leq E_{\mathrm{th}} \leq 80\ \mathrm{EeV}$) and over the angular scale ($1° \leq \psi \leq 30°$). We also consider different maximum distances to the objects, D, scanning on this from 10 Mpc up to 200 Mpc, in steps of 10 Mpc. To find excesses of pairs we compare their observed number with that resulting from isotropic simulations. For each considered distance D we first calculate the fraction of isotropic simulations having an equal number to or more pairs than the data, $f(\psi, E_{\mathrm{th}})$, and then we look for its minimum, f_{min}. The post-trial probability, P, is calculated as the fraction of isotropic simulations which, under similar scans over E_{th} and ψ for each considered D, lead to a value of f_{min} smaller than the one obtained with the data.

Figure 5 displays the results for the case of the 2MRS catalog. The top-left panel shows f_{min} (asterisks) and P (squares) obtained for each distance D. The minimum values are observed for $D = 90$ Mpc, for which $f_{\mathrm{min}} \simeq 1.5 \times 10^{-3}$ and $P \simeq 8\%$. The top-right panel in the figure shows the distribution of $f(\psi, E_{\mathrm{th}})$ as a function of energy threshold and angle for the value $D = 90$ Mpc giving rise to the minimum probability. The local minimum (indicated with a cross) is observed for $\psi = 9°$ and $E_{\mathrm{th}} = 52$ EeV. For these values, 20,042 pairs are expected on average from isotropic realizations while 23,101 are observed in the data. Considering the penalization due to the scan in D performed, the probability $\mathcal{P}$ to obtain a value of P smaller than 8\% from isotropic distributions for any value of D is $\mathcal{P} \simeq 24\%$. Finally, the bottom panel of the figure displays the map of the events with $E \geq 52$ EeV (black dots). Also drawn is a blue fuzzy circle around each 2MRS galaxy closer than 90 Mpc. All of those circles have radius $9°$, which is the value for which the cross-correlation has maximum significance. Given the very large number of galaxies in 2MRS, essentially all events are within $9°$ of at least one galaxy. Events falling in regions of the plot with denser color will have more galaxies within $9°$ and hence will contribute more pairs to the cross-correlation at this angular scale.

Similar plots to those presented above are included in Figure 6 for the case of the Swift-BAT catalog. As shown in the top-left panel of the figure, the minimum values are reached here for $D = 80$ Mpc, where $f_{\mathrm{min}} \simeq 6 \times 10^{-5}$ and $P \simeq 1\%$. Correspondingly, the top-right panel in the figure shows $f(\psi, E_{\mathrm{th}})$ as a function of energy and angle at $D = 80$ Mpc. The local minimum (indicated with a cross) is at $\psi = 1°$ and $E_{\mathrm{th}} = 58$ EeV, where 9 pairs are observed and 1.6 are expected on average. After accounting for the
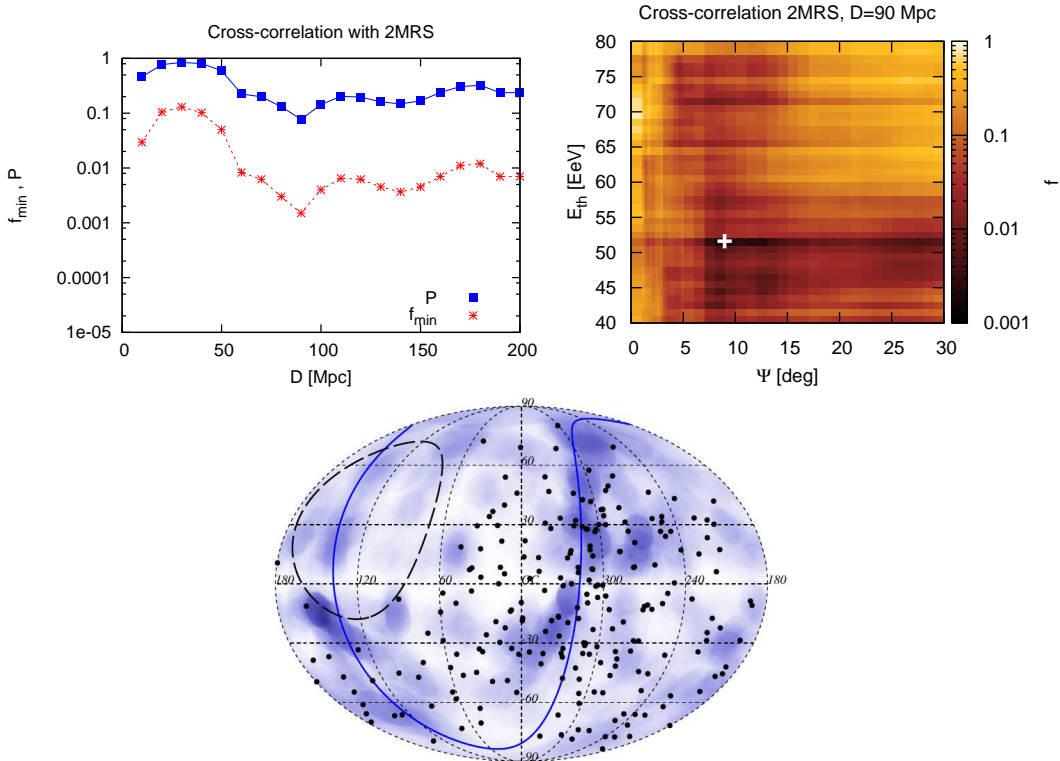
Fig. 5.— Cross-correlation of events with the galaxies in the 2MRS catalog. The top-left panel shows the values of f_{min} and P as a function of the maximum distance D to the galaxies considered. The top-right panel shows the results of the scan in ψ and E_{th} for the value $D = 90$ Mpc corresponding to the minimum values in the top-left plot. The bottom plot shows the sky distribution (in Galactic coordinates) of the events with $E \geq 52$ EeV (black dots). Blue fuzzy circles of 9° radius are drawn around all of the 2MRS objects closer than 90 Mpc. The dashed line is the field-of-view limit for the Auger Observatory (for $\theta \leq 80°$) and the blue solid line corresponds to the Super-Galactic Plane.

penalization due to the scan performed in D, the probability of obtaining a value of P smaller than 1% from isotropic distributions for any value of D is $\mathcal{P} \simeq 6\%$. Finally, we show the map of events and objects in the bottom panel. Given the minimum found, we include events with $E \geq 58$ EeV and draw circles of 1° radius around the BAT AGNs closer than 80 Mpc.

The results of the cross-correlation with jetted radio galaxies are shown in Figure 7. The minimum value $f_{min} \simeq 2 \times 10^{-4}$, with $P \simeq 1.4\%$, is obtained for $D = 10$ Mpc (see top-left panel). The only object included in this catalog within such a distance is the Centaurus A galaxy. Since the correlation with Cen A is discussed separately in the next section, we consider here the second minimum, which is found for $D = 90$ Mpc. This
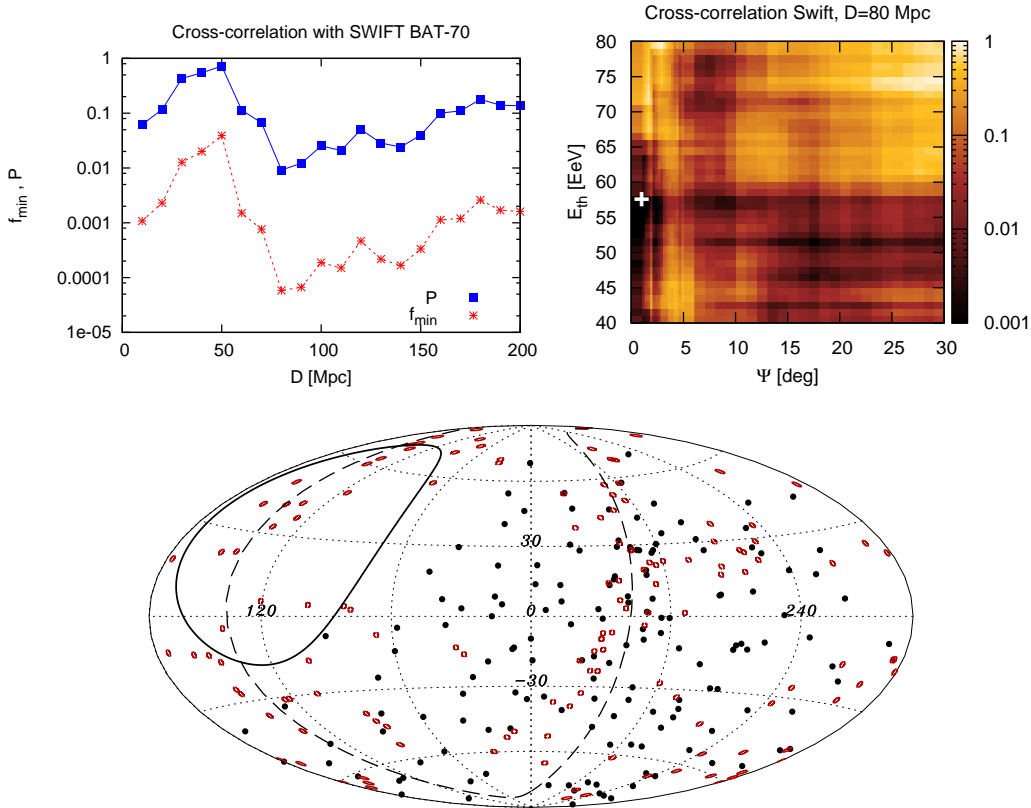
Fig. 6.— Cross-correlation of events with the AGNs in the Swift-BAT catalog. The top-left panel shows the values of $f_{\min}$ and P as a function of the maximum distance D to the AGNs considered. The top-right panel shows the results of the scan in ψ and E_{th} for the value $D = 80$ Mpc corresponding to the minimum values in the top-left plot. The bottom plot shows the sky distribution (in Galactic coordinates) of the events with $E \geq 58$ EeV (black dots). Red circles of 1° radius are drawn around the BAT AGNs closer than 80 Mpc.

minimum corresponds to $f_{\min} \simeq 4 \times 10^{-4}$ and $P \simeq 3.4\%$. The top-right panel in the figure thus shows the results of the scan in angle and energy for $D = 90$ Mpc. The minimum occurs for $\psi = 4.75°$ and $E_{\mathrm{th}} = 72$ EeV, where 13 pairs are observed in the data and 3.2 are expected on average. The chance probability for getting $P \leq 1.4\%$ (corresponding to the absolute minimum found) for any value of D is $\mathcal{P} \simeq 8\%$. As was done for the other catalogs, the bottom panel displays the map of events and objects corresponding to the minimum found, i.e., $E \geq 72$ EeV and $D = 90$ Mpc. Circles of radius 4.75° are drawn around every radio galaxy and the events are indicated with black dots.

While the cross-correlation analysis does not provide us with a significant indication of excesses of pairs with any of the catalogs considered, at any energy, distance and angle, we note that all of them yield minima for similar maximum distances to the objects ($\sim$80
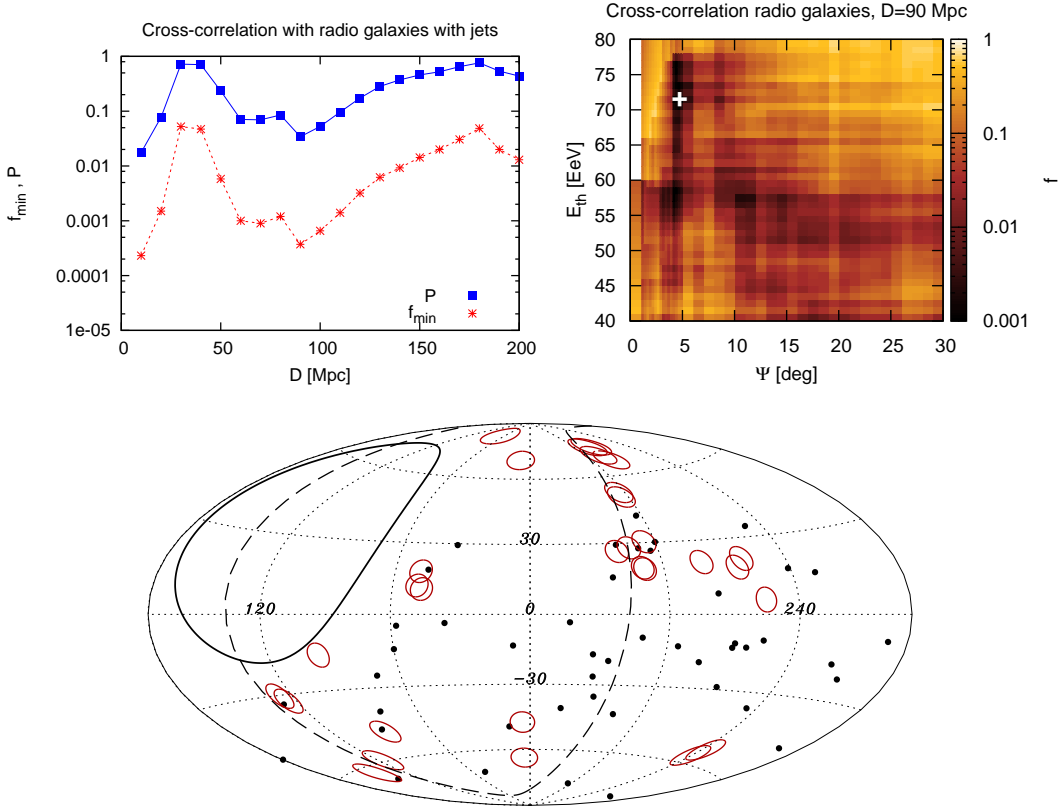
Fig. 7.— Cross-correlation of events with the AGNs in the catalog of radio galaxies with jets. The top-left panel shows the values of f_{min} and P as a function of the maximum distance D to the AGNs considered. The top-right panel shows the results of the scan in ψ and E_{th} for the value $D = 90$ Mpc corresponding to the (second) minimum in the top-left plot. The bottom plot shows the sky distribution (in Galactic coordinates) of the events with $E \geq 72$ EeV (black dots). Red circles of 4.75° radius are drawn around the radio galaxies closer than 90 Mpc.

to 90 Mpc) although for different threshold energies and angular scales. The fact that the distances are similar for the three catalogs is actually expected given the existing correlations between catalogs, since AGNs are preferentially located in regions of high density of galaxies. On the other hand, the preference towards $D \simeq 80$ Mpc is mostly due to the fact that for this value the whole Centaurus Supercluster gets included and in this region there is an excess of high-energy events.

6.2. Cross-Correlation with Bright AGNs

We present here the results of a scan over the minimum source luminosities, considering for the Swift AGNs the reported X-ray band luminosity $\mathcal{L}_X$ and for the radio-galaxy sample the reported radio luminosity $\mathcal{L}_R$, computed per logarithmic energy bin at 1.1 GHz. For Swift we scan from $\mathcal{L}_X = 10^{42}$ erg/s up to 10^{44} erg/s, while for the radio galaxies we scan from $\mathcal{L}_R = 10^{39}$ erg/s up to 10^{41} erg/s, considering three logarithmic steps per decade, for a total of 7 luminosity values in each case. These luminosity values cover most of the range spanned by the actual luminosities of the AGNs that are present in the catalogs (just 10 AGNs from the Swift sample have $\mathcal{L}_X < 10^{42}$ erg/s, while only 3 AGNs from the radio-galaxy sample have $\mathcal{L}_R < 10^{39}$ erg/s). Given the additional scan performed in $\mathcal{L}$, we do a slightly coarser scan in D, using 20 Mpc steps to cover from 10 Mpc up to 190 Mpc.
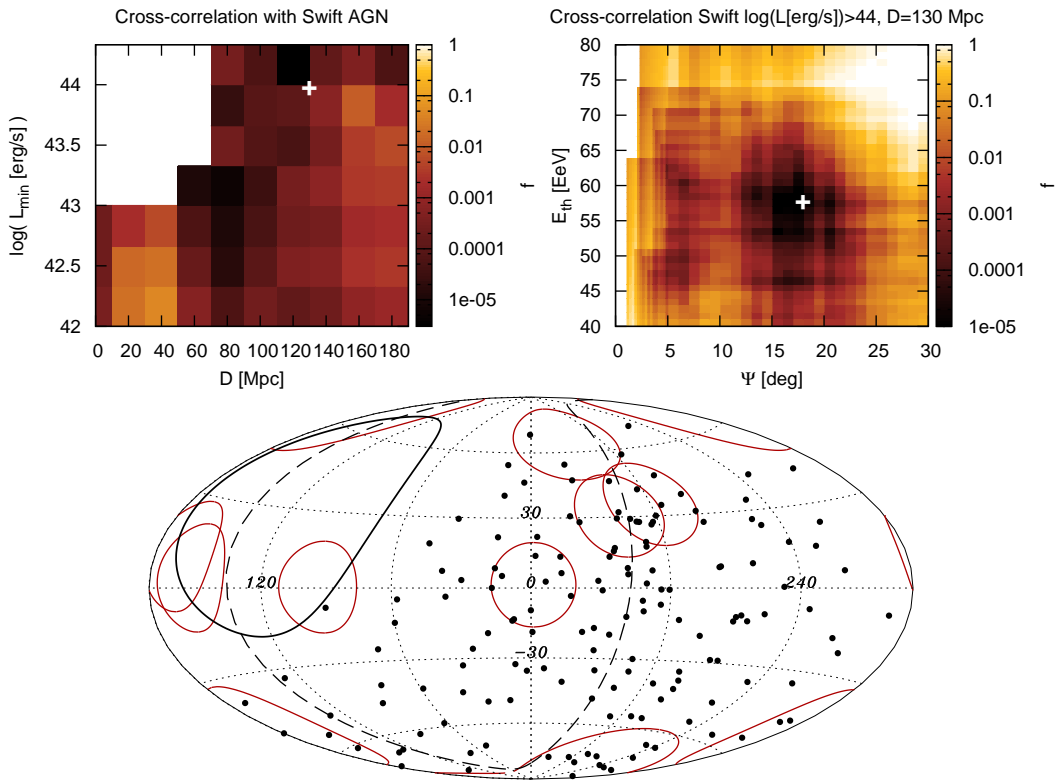

Fig. 8.— Cross-correlation of events with the AGNs in the Swift catalog as a function of D and $\mathcal{L}_{\min}$ (top-left panel) and detail of the scan in Ψ and $E_{\rm th}$ for the minimum found (top-right panel). The bottom map (in Galactic coordinates) shows the events with $E \geq 58$ EeV together with the Swift AGNs brighter than 10^{44} erg/s and closer than 130 Mpc, indicated with red circles of 18° radius.

Considering first the Swift catalog, we show in the top-left panel of Figure 8 the

resulting values of $f_{\min}$ as a function of the maximum AGN distance and the minimum adopted luminosity $\mathcal{L}_{\min}$ in the respective bands (the white region in the top-left corner of the plot is due to the absence of nearby objects above those luminosity thresholds). The values of $f_{\min}$ are obtained after scanning on Ψ and E_{th} as in the previous subsection. The minimum value of $f_{\min} = 2{\times}10^{-6}$ is obtained for $D = 130$ Mpc and $\mathcal{L} > 10^{44}$ erg/s. The top-right panel shows the details of the scan in Ψ and E_{th} for $D = 130$ Mpc and $\mathcal{L} > 10^{44}$ erg/s. The minimum corresponds to the values $\Psi = 18°$ and $E_{\mathrm{th}} = 58$ EeV. For these parameters there are 10 AGNs and 155 events, and 62 pairs are obtained between them while the isotropic expectation is 32.8. The probability to find values $f_{\min} < 2{\times}10^{-6}$ in isotropic simulations after making the same scan on Ψ, E_{th}, $\mathcal{L}_{\min}$ and D is $\mathcal{P} \simeq 1.3\%$.

The bottom plot in the figure is the map of events with $E \geq 58$ EeV (black dots) and the Swift AGN brighter than 10^{44} erg/s that are closer than 130 Mpc, represented in the map with red circles of $18°$ radius, which is the value of Ψ found at the minimum. We see that the events that mostly contribute to the excess of pairs observed are those arriving from directions contained inside the circles centered on IC 4329A (at $(\ell, b) = (317.6°, 30.9°)$), ESO 506-G027 (at $(\ell, b) = (299.6°, 35.5°)$), AX J1737.4-2907 (at $(\ell, b) = (358.9°, 1.4°)$), NGC 612 (at $(\ell, b) = (261.8°, -77°)$) and NGC 1142 (at $(\ell, b) = (175.9°, -49.9°)$)[6].

Figure 9 is similar but for the sample of radio galaxies. The scan in luminosity leads to two minima with very similar probabilities, both for $D = 90$ Mpc (see the top-left panel). The first one has $f_{\min} = 5.1{\times}10^{-5}$ and corresponds to $\mathcal{L} > 10^{39.33}$ erg/s, $\Psi = 4.75°$ and $E_{\mathrm{th}} = 72$ EeV, the angle and energy being equal to the parameters already obtained in the previous subsection (Figure 7). The main difference is that 32 AGNs remain within 90 Mpc once the luminosity cut is imposed, compared to the original sample of 39 AGNs in the flux-limited sample, so that the expected number of pairs becomes 2.4 while 13 are actually observed. The second minimum has $f_{\min} = 5.6{\times}10^{-5}$ and corresponds to $\mathcal{L} > 10^{40}$ erg/s. The top-right panel shows the scan in Ψ and E_{th} for this minimum, which leads to $\Psi = 12°$ and $E_{\mathrm{th}} = 58$ EeV. The bottom plot shows the map of the arrival directions of the events with $E \geq 58$ EeV (black dots) and the radio galaxies within 90 Mpc, indicated with red circles of $12°$ radius. We see that most of the excess in the number of pairs arises from the events falling in the circles around the radio galaxies in the Centaurus region. The globally penalized probability of getting $f_{\min} < 5.1{\times}10^{-5}$ after a similar scan with the radio galaxies turns out to be in this case $\mathcal{P} \simeq 11\%$.

---

[6] One of the objects in the sample of 10 AGNs is the BLLac Mrk 421, a powerful gamma-ray emitter at $(\ell, b) = (179.9°, 65°)$, which has been proposed as a candidate source for the hot spot observed by the Telescope Array (Fang et al. 2014). This object is in a low-exposure region near the border of the Auger field of view, and there are no events with $E > 58$ EeV within $18°$ of it.
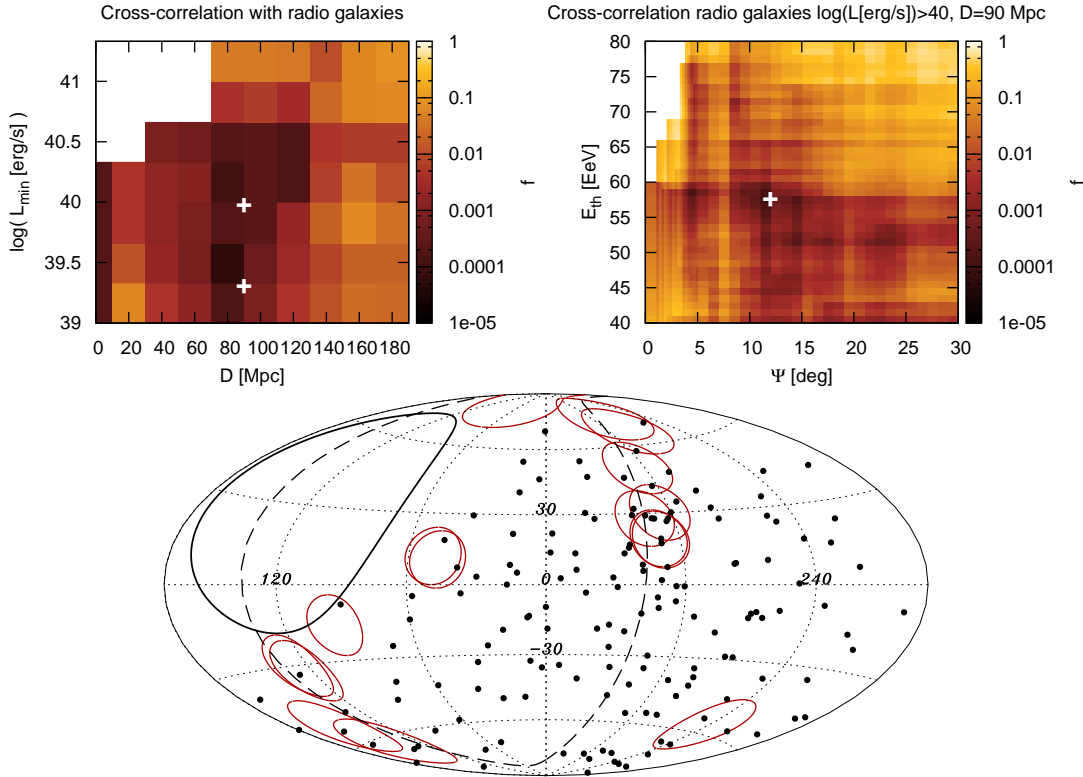
Fig. 9.— Cross-correlation of events with the radio galaxies as a function of D and $\mathcal{L}_{\min}$ (top-left panel) and detail of the scan in Ψ and $E_{\rm th}$ for the second minimum found (top-right panel). The bottom map (in Galactic coordinates) shows the events with $E \geq 58$ EeV together with the radio galaxies brighter than 10^{40} erg/s and closer than 90 Mpc, indicated with red circles of $12°$ radius (i.e., the parameters of the second minimum).

7. The Centaurus A Region

Centaurus A is the nearest radio-loud active galaxy, at a distance of less than 4 Mpc. It is thus an obvious candidate source of UHECRs in the southern sky (Romero et al. 1996). In addition, the nearby Centaurus cluster is a large concentration of galaxies lying in approximately the same direction and at a distance of ∼50 Mpc. The most significant localized excess of UHECR arrival directions reported earlier by the Pierre Auger Collaboration (Abreu et al. 2010) was very close to the direction of Cen A. In particular, we found 13 events with energy above 55 EeV in a circular window of radius $18°$ centered on Cen A, while 3.2 were expected in case of isotropy[7]. As shown in Section 4.1,

---

[7]We note however that the significance of the excess in this particular window of $18°$ and for the rescaled energy threshold of 53 EeV did not grow with the additional data included in this work, for which

the most significant excess observed in a blind search over the exposed sky with the present data set is also a region close to the direction of Cen A.
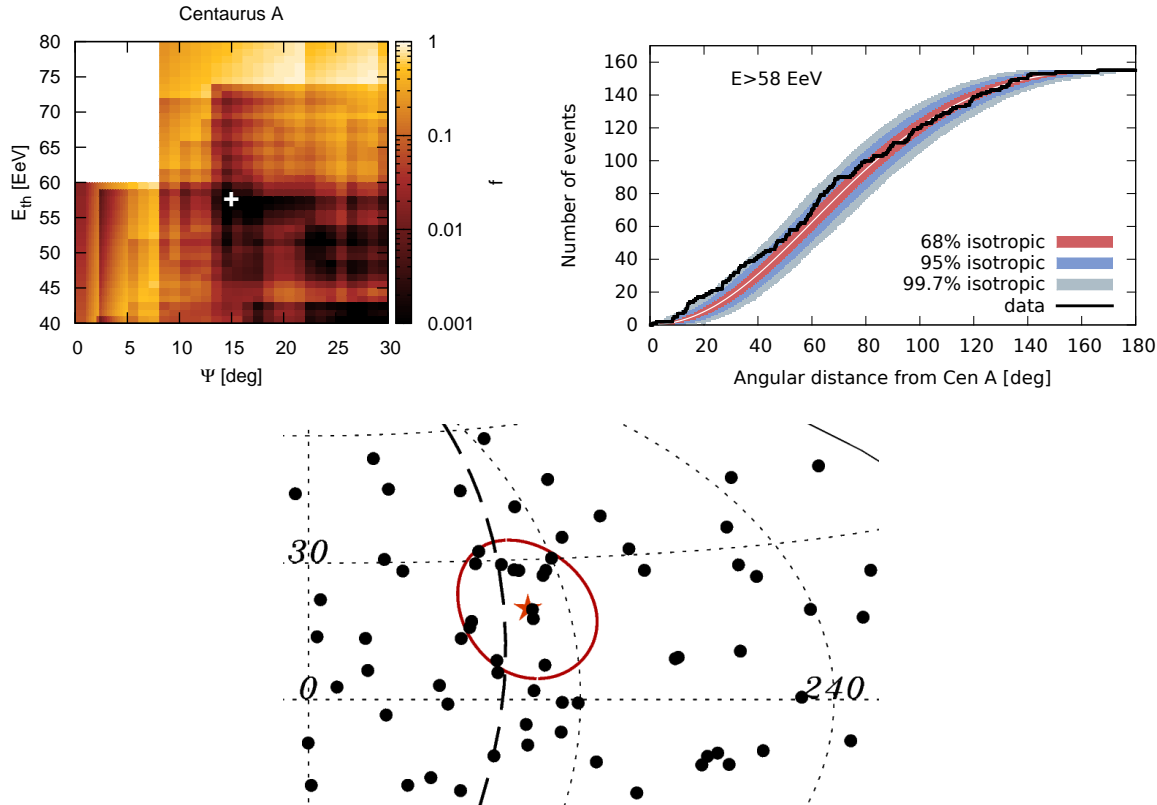

Fig. 10.— Correlation of events with the Cen A radio galaxy as a function of the angular distance and the energy threshold, E_{th} (top-left panel). The top-right panel shows the cumulative number of events for the threshold $E_{\mathrm{th}} = 58$ EeV, exploring the whole angular range. The bottom panel displays the map (in Galactic coordinates) of the region around Centaurus A, showing the arrival directions of the events with $E \geq 58$ EeV (black dots) and a red circle of $15°$ radius around the direction of Cen A, indicated by a star.

In this section we search for cross-correlations of the arrival directions with the direction of Cen A, $(\ell, b) = (-50.5°, 19.4°)$. The search is performed by varying the energy threshold of events between 40 EeV and 80 EeV and by counting events in angular radii ranging from $1°$ to $30°$. To assess the significance of the observed number of events, we compare it to the one expected from isotropic simulations based on the same number of arrival directions as in the data. Figure 10 (top-left panel) shows the fraction f of those simulations that yield more than or an equal number of pairs to the data. The minimum

$n_{\mathrm{obs}}/n_{\mathrm{exp}} = 18/9$.

value of f is $f_{\min} = 2 \times 10^{-4}$, corresponding to $E_{\rm th} = 58$ EeV and $\psi = 15°$. There are 14 events (out of a total of 155) observed while 4.5 are expected on average from isotropic distributions. The fraction of isotropic simulated data sets that yield a smaller value of $f_{\min}$ under a similar scan is $\mathcal{P} \simeq 1.4\%$. For completeness, we show in the top-right panel of the figure the number of events with energy above 58 EeV as a function of the angular distance from Cen A for the whole angular range, indicating also the 68, 95 and 99.7% ranges obtained with isotropic simulations. The bottom panel displays the map in Galactic coordinates of the Centaurus A region, showing the events with $E \geq 58$ EeV (black dots) and a $15°$ radius circle around the direction of Cen A, indicated by a star.

8. Discussion

We have presented several tests to search for signals of anisotropies in the arrival directions of the highest-energy events detected by the Pierre Auger Observatory from 2004 January 1 up to 2014 March 31. The main results obtained are summarized below.

We first updated the fraction of events with energy above 53 EeV correlating with AGNs in the VCV catalog, obtaining a value of $28.1^{+3.8}_{-3.6}\%$, to be compared with 21% for the isotropic expectation. This test then does not yield significant evidence of anisotropies above this particular energy threshold. Consequently, in all other exploratory analyses performed we have considered the data set down to an energy of 40 EeV.

A thorough search for overdense circular regions all over the sky and for different threshold energies led to the largest deviation from isotropy in a $12°$ radius window centered at $(\alpha, \delta) = (198°, -25°)$ and for events with energies above 54 EeV, but more significant excesses are obtained in 69% of isotropic simulations under a similar scan. The autocorrelation of the events was also found to be compatible with the expectations from an isotropic distribution.

No significant excesses were found around the Galactic Center, the Galactic Plane, or the Super-Galactic Plane. This suggests that, if the deflections are not too large, at these energies the sources are unlikely to be Galactic and also that a non-negligible fraction of the flux arises from extragalactic sources that are not very close to the Super-Galactic Plane.

The high degree of isotropy observed in all these tests of the distribution of UHECRs is indeed quite remarkable, certainly challenging original expectations that assumed only few cosmic ray sources with a light composition at the highest energies. If the actual source distribution were anisotropic, these results could be understood for instance as due to the large deflections caused by the intervening magnetic fields if a large fraction of the CRs in this energy range were heavy, as is indeed suggested by mass-composition studies

(Abraham et al. 2010a; Aab et al. 2014). Alternatively, it could also be explained in a scenario in which the number of individual sources contributing to the CR fluxes is large. Indeed, the lack of autocorrelation has been used in Abreu et al. (2013a) to set lower bounds on the density of sources if the deflections involved are not large.

We have also studied the cross-correlation between events and nearby extragalactic objects in different flux-limited catalogs with the aim of identifying possible scenarios of UHECR sources. The parameters corresponding to the minima obtained when scanning in energy, distance and angular scale are listed in Table 1 (first three rows). The penalized probabilities that these minima are due to fluctuations of an isotropic background are of the order of a few percent. In all three cases the object distance corresponding to the minima is $D \simeq 80$ to 90 Mpc, although it happens for different angular scales and energy thresholds. When a further scan is performed on the minimum intrinsic AGN luminosity, additional minima appear (see rows 4 and 5 in Table 1). We note that the penalized probability is $\sim 1.3\%$ for Swift AGNs within 130 Mpc and brighter than 10^{44} erg/s, corresponding to an excess of pairs for events above 58 EeV on angular scales of $18°$, while for the radio galaxies the penalized probability is $\sim 11\%$.

Objects	E_{th} [EeV]	Ψ [°]	D [Mpc]	$\mathcal{L}_{\min}$ [erg/s]	$f_{\min}$	$\mathcal{P}$
2MRS Galaxies	52	9	90	-	1.5×10^{-3}	24%
Swift AGNs	58	1	80	-	6×10^{-5}	6%
Radio galaxies	72	4.75	90	-	2×10^{-4}	8%
Swift AGNs	58	18	130	10^{44}	2×10^{-6}	1.3%
Radio galaxies	58	12	90	$10^{39.33}$	5.6×10^{-5}	11%
Centaurus A	58	15	-	-	2×10^{-4}	1.4%

Table 1: Summary of the parameters of the minima found in the cross-correlation analyses.

Finally, considering circular windows around the direction of Cen A, the most significant indication of anisotropy appears for events with $E \geq 58$ EeV and for an angular radius of $15°$. After penalizing for the scan on the angle and energy threshold this has a 1.4% probability of arising by chance from an isotropic distribution. Clearly the events contributing to the excess around the direction of Cen A also contribute to the signals found in the cross-correlation searches performed against the different catalogs, which in general have an excess of objects in directions close to that of Cen A.

Overall, none of the tests performed yields a statistically significant evidence of anisotropy in the distribution of UHECRs. It will be in any case interesting to follow with future data the evolution of the excesses found in the cross-correlation studies, particularly from Cen A and from the bright AGNs. If the present level of correlations were maintained in independent data sets, the most efficient test for anisotropy would be the

one that led to the smallest value of $f_{\min}$ at present, i.e., that of the cross-correlation within 18° of the events with energy above 58 EeV and the Swift AGNs lying within 130 Mpc and brighter than 10^{44} erg/s.

Acknowledgments

REFERENCES

Aab, A., Abreu, P., Aglietta, M., et al. (The Pierre Auger Collaboration) 2013, ArXiv e-prints, arXiv:1307.5059

—. 2014, J. Cosmology Astropart. Phys., 8, 19

—. 2014, ArXiv e-prints, arXiv:1409.4809, Phys. Rev. D, in press

—. 2014, ArXiv e-prints, arXiv:1409.5083, Phys. Rev. D, in press

Abbasi, R. U., Abu-Zayyad, T., Allen, M., et al. 2008, PhRvL, 100, 101101

Abbasi, R. U., Abu-Zayyad, T., Al-Seady, M., et al. 2010, PhRvL, 104, 161101

Abbasi, R. U., Abe, M., Abu-Zayyad, T., et al. 2014a, ArXiv e-prints, arXiv:1404.5890

—. 2014b, ArXiv e-prints, arXiv:1408.1726

Abraham, J., Aglietta, M., Aguirre, I. C., et al. (The Pierre Auger Collaboration) 2004, NIMPA, 523, 50

Abraham, J., Abreu, P., Aglietta, M., et al. (The Pierre Auger Collaboration) 2007, Science, 318, 938

—. 2008a, APh, 29, 188

—. 2008b, PhRvL, 101, 061101

—. 2009, APh, 31, 399

—. 2010a, PhRvL, 104, 091101

—. 2010b, NIMPA, 613, 29

Abreu, P., Aglietta, M., Ahlers, M., et al. (The Pierre Auger Collaboration) 2013a, J. Cosmology Astropart. Phys., 5, 9

Abreu, P., Aglietta, M., M., A., et al. (The Pierre Auger Collaboration) 2013b, J. Cosmology Astropart. Phys., 1302, 026

Abreu, P., Aglietta, M., Ahn, E. J., et al. (The Pierre Auger Collaboration) 2010, APh, 34, 314

—. 2011, ArXiv e-prints, arXiv:1107.4809

Abu-Zayyad, T., Aida, R., Allen, M., et al. 2013, ApJ, 768, L1

Ave, M., Bohacova, M., Curry, E., et al. 2013, APh, 42, 90

Ave M. for the Pierre Auger Collaboration 2007, Proceedings of the 30th International Cosmic Ray Conference, 4, 307, ArXiv e-prints, arXiv:0709.2125

Baumgartner, W. H., Tueller, J., Markwardt, C. B., et al. 2013, ApJS, 207, 19

Bonifazi, C for The Pierre Auger Collaboration 2009, Nucl. Phys. B Proc. Suppl., 190, 20

Condon, J. J., Cotton, W. D., Greisen, E. W., et al. 1998, AJ, 115, 1693

Fang, K., Fujii, T., Linden, T., & Olinto, A. V. 2014, ApJ, 794, 126

Farrar, G. R. 2014, Comptes Rendus Physique, 15, 339

Farrar, G. R., & Gruzinov, A. 2009, ApJ, 693, 329

Greisen, K. 1966, PhRvL, 16, 748

Harari, D., Mollerach, S., & Roulet, E. 2006, J. Cosmology Astropart. Phys., 11, 12

Huchra, J. P., Macri, L. M., Masters, K. L., et al. 2012, ApJS, 199, 26

Kampert, K.-H. for the Pierre Auger Collaboration 2012, 32nd International Cosmic Ray Conference (2011), 12, 32

Li, T.-P., & Ma, Y.-Q. 1983, ApJ, 272, 317

Mauch, T., Murphy, T., Buttery, H. J., et al. 2003, MNRAS, 342, 1117

Romero, G. E., Combi, J. A., Perez Bergliaffa, S. E., & Anchordoqui, L. A. 1996, APh, 5, 279

Tueros, M. for the Pierre Auger Collaboration 2013, ArXiv e-prints, arXiv:1307.5059

Van Velzen, S., Falcke, H., Schellart, P., Nierstenhöfer, N., & Kampert, K.-H. 2012, A&A, 544, A18

Veron-Cetty, M.-P., & Veron, P. 2006, A&A, 455, 773

Verzi, V., for the Pierre Auger Collaboration 2013, ArXiv e-prints, arXiv:1307.5059

Zatsepin, G., & Kuzmin, V. 1966, JETPL, 4, 78

A.   LIST OF EVENTS

In this Appendix we give the arrival directions and energies of the 231 events[8] with $E \geq 52$ EeV and $\theta < 80°$ detected by the Pierre Auger Observatory from 2004 January 1 up to 2014 March 31. The threshold has been chosen so that it includes all of the events leading to the minimal probabilities in the cross-correlation studies performed with the different catalogs. The information about these events is collected in Table 2. The different columns are: year, Julian day for that year, zenith angle, energy, right ascension, declination, Galactic longitude and Galactic latitude.

Figure 11 displays the arrival directions of these events in Galactic coordinates. The dark filled circles correspond to the events in the vertical sample ($\theta \leq 60°$) while the white filled circles correspond to those in the inclined sample ($60° < \theta < 80°$). The size of the circles scales with the energy of the events. The background color in the map indicates the relative exposure of the Auger Observatory to different declinations. The white region is outside the field of view of the Auger Observatory for $\theta < 80°$.
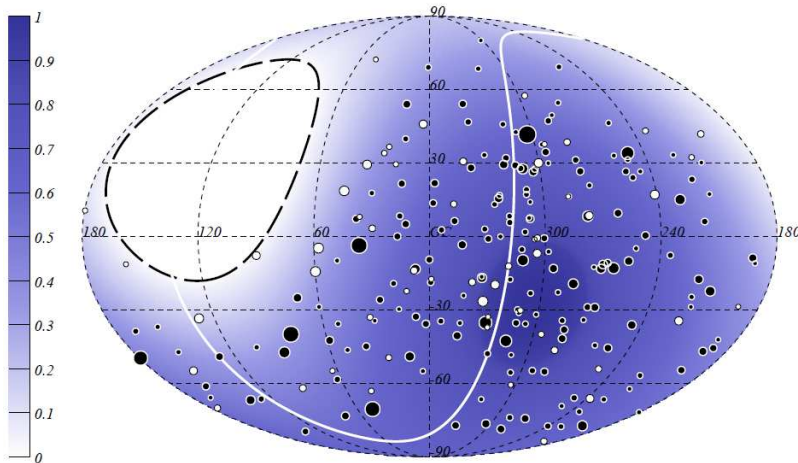
Fig. 11.— Map in Galactic coordinates of the arrival directions of the events with $E \geq 52$ EeV. The black (white) circles correspond to *vertical* (*inclined*) events. The size of each circle scales with the energy of the event. The color scale is proportional to the relative exposure.

---

[8]We note that out of the 69 events published in Abreu et al. (2010), 5 turn out to have energies below 52 EeV with the present reconstruction and hence they do not appear in the table.

Table 2.   List of the events with energies above 52 EeV and $\theta < 80°$, the columns being: year, day, zenith angle θ, energy E, right ascension α, declination δ and Galactic longitude ℓ and latitude b.

Year	Julian day	θ [°]	E [EeV]	α [°]	δ [°]	ℓ [°]	b [°]
2004	125	47.7	62.2	267.2	−11.4	15.5	8.4
2004	142	59.2	84.7	199.7	−34.9	−50.8	27.7
2004	177	71.5	54.6	12.7	−56.6	−56.9	−60.5
2004	239	58.3	54.0	32.7	−85.0	−59.1	−31.8
2004	282	26.3	58.6	208.1	−60.1	−49.5	1.9
2004	339	44.6	78.2	268.4	−61.0	−27.6	−16.9
2004	343	23.3	58.2	224.7	−44.0	−34.1	13.1
2005	50	67.5	60.2	29.0	−14.0	174.9	−70.0
2005	54	34.9	71.2	17.5	−37.8	−76.0	−78.6
2005	63	54.4	71.9	331.2	−1.3	58.7	−42.4
2005	81	17.1	52.1	199.1	−48.5	−52.8	14.1
2005	186	57.5	108.2	45.6	−1.7	179.5	−49.6
2005	233	65.4	61.9	278.4	−1.3	29.7	3.4
2005	295	15.3	54.9	333.0	−38.1	4.4	−55.0
2005	306	14.2	74.9	114.8	−42.8	−103.9	−10.0
2005	347	65.6	77.5	18.3	29.2	128.6	−33.4
2006	5	30.9	78.2	18.9	−4.7	138.3	−66.8
2006	35	30.8	72.2	53.6	−7.8	−165.9	−46.9
2006	55	37.9	52.8	267.6	−60.6	−27.5	−16.4
2006	64	66.6	64.8	275.2	−57.2	−22.6	−18.6
2006	81	34.0	69.5	201.1	−55.3	−52.3	7.3
2006	100	33.7	54.7	28.8	−16.4	−179.9	−71.8
2006	118	57.3	56.3	322.5	−2.0	51.6	−35.6
2006	126	65.2	82.0	299.0	19.4	57.6	−4.7
2006	142	22.6	64.3	121.8	−52.5	−93.0	−10.7
2006	160	76.5	60.7	52.7	−43.4	−109.6	−54.1
2006	185	58.8	89.0	349.9	9.3	88.4	−47.3
2006	263	49.9	53.0	82.1	14.6	−169.9	−10.9
2006	284	54.5	54.0	142.3	−13.1	−114.3	26.6
2006	296	53.9	67.7	53.0	−4.5	−170.5	−45.6
2006	299	26.0	59.5	200.9	−45.3	−51.2	17.2
2006	350	17.6	60.0	305.6	−46.3	−6.4	−34.5
2007	9	54.0	53.8	321.0	8.1	60.4	−28.7
2007	13	14.2	127.1	192.8	−21.2	−57.1	41.7
2007	14	55.9	52.2	192.6	17.2	−58.4	80.1
2007	69	30.4	60.0	200.2	−43.4	−51.4	19.2
2007	84	17.5	60.8	143.4	−18.1	−109.4	24.1
2007	106	49.8	70.3	17.5	13.6	129.8	−49.0

Table 2—Continued

Year	Julian day	θ [°]	E [EeV]	α [°]	δ [°]	ℓ [°]	b [°]
2007	145	24.0	68.4	47.5	−12.8	−164.0	−54.5
2007	161	41.9	53.6	137.3	6.2	−135.9	33.4
2007	166	79.6	54.9	245.8	8.5	22.9	36.7
2007	186	44.9	61.5	219.5	−53.9	−41.7	5.8
2007	193	17.9	79.7	325.5	−33.4	12.2	−49.0
2007	203	55.3	57.0	265.9	5.9	30.5	17.8
2007	205	76.5	61.9	195.5	−63.4	−55.9	−0.6
2007	221	35.5	67.8	212.8	−3.1	−21.6	54.2
2007	227	33.6	60.7	192.5	−35.3	−57.3	27.5
2007	234	33.3	68.1	185.3	−27.9	−65.2	34.5
2007	235	42.6	60.8	105.9	−22.9	−125.2	−7.7
2007	295	21.1	65.9	325.7	−15.5	37.8	−44.8
2007	295	56.5	55.8	39.2	19.4	154.4	−36.9
2007	314	76.7	52.5	59.6	38.3	158.5	−11.3
2007	339	68.2	54.0	250.3	1.8	18.5	29.5
2007	343	30.9	82.4	81.6	−7.4	−150.1	−22.3
2007	345	51.6	72.7	315.3	−53.8	−16.0	−40.5
2008	10	77.1	80.2	271.1	19.0	45.2	18.7
2008	13	16.8	64.2	252.7	−22.7	−1.9	13.7
2008	18	50.2	111.8	352.6	−20.8	47.5	−70.5
2008	36	28.3	65.3	187.5	−63.5	−59.5	−0.7
2008	48	76.9	60.4	19.8	−25.5	−160.1	−83.6
2008	49	50.7	56.0	64.1	−52.7	−98.5	−44.4
2008	51	20.7	53.3	202.0	−54.9	−51.8	7.6
2008	52	31.7	56.2	82.8	−15.8	−141.2	−24.7
2008	72	4.4	52.4	184.4	−32.4	−65.2	30.0
2008	87	38.9	73.1	220.6	−42.8	−36.3	15.5
2008	118	36.2	62.9	110.2	−0.9	−142.9	6.1
2008	142	43.4	56.7	199.4	6.6	−39.0	68.5
2008	184	53.7	55.7	33.0	11.0	152.8	−47.2
2008	192	20.2	55.1	306.5	−55.1	−17.1	−35.3
2008	205	53.1	56.7	358.9	15.5	103.6	−45.2
2008	250	68.8	52.0	67.7	4.0	−168.7	−28.6
2008	264	44.4	89.3	116.0	−50.6	−96.4	−12.9
2008	266	59.0	61.2	339.4	−63.3	−35.4	−47.8
2008	268	49.8	118.3	287.7	1.5	36.5	−3.6
2008	282	29.0	58.1	202.2	−16.1	−44.2	45.9
2008	296	42.8	64.7	15.6	−17.1	137.9	−79.6

Table 2—Continued

Year	Julian day	θ [°]	E [EeV]	α [°]	δ [°]	ℓ [°]	b [°]
2008	322	28.4	62.2	25.0	−61.4	−67.1	−54.8
2008	328	47.2	63.1	126.4	5.3	−140.8	23.4
2008	329	47.9	66.9	28.9	−2.7	157.9	−61.2
2008	331	50.7	52.6	304.4	−26.2	16.7	−29.6
2008	337	30.8	65.8	275.2	−14.4	16.7	0.1
2008	355	71.7	71.1	196.1	−69.7	−55.9	−6.9
2008	362	31.5	74.0	209.6	−31.3	−40.7	29.4
2009	7	59.2	61.0	286.3	−37.8	−0.6	−18.7
2009	30	32.3	66.2	303.9	−16.5	26.8	−25.8
2009	32	56.2	70.3	0.0	−15.4	75.0	−73.2
2009	35	52.8	57.7	227.0	−85.2	−54.2	−23.1
2009	39	42.4	64.1	147.2	−18.3	−106.5	26.6
2009	47	20.7	52.9	78.3	−16.0	−142.9	−28.8
2009	51	6.9	66.7	203.4	−33.0	−47.0	29.1
2009	73	37.0	72.5	193.8	−36.4	−56.2	26.5
2009	78	27.2	74.4	122.7	−54.7	−90.7	−11.4
2009	78	8.2	59.0	26.7	−29.1	−134.5	−77.6
2009	80	18.4	65.8	251.4	−35.8	−13.0	6.3
2009	80	44.4	63.8	170.1	−27.4	−80.8	31.3
2009	83	68.6	56.2	249.1	9.1	25.3	34.1
2009	140	27.2	55.1	330.8	−8.9	49.5	−46.3
2009	160	40.9	52.8	43.9	−25.4	−143.4	−62.2
2009	162	78.2	70.5	39.4	−34.5	−122.6	−66.1
2009	163	41.2	71.9	23.3	−40.2	−87.9	−74.3
2009	172	9.7	65.8	276.1	−33.4	0.1	−9.4
2009	191	26.9	59.5	294.5	−20.5	19.1	−19.2
2009	197	51.7	52.2	129.4	15.2	−149.5	30.2
2009	202	60.8	63.6	358.2	−2.8	90.4	−61.9
2009	212	52.7	55.3	122.5	−78.5	−68.8	−22.8
2009	219	40.1	53.2	29.4	−8.6	166.2	−65.8
2009	219	59.7	58.3	304.3	−81.9	−48.3	−29.8
2009	237	78.4	70.0	325.8	42.8	90.1	−7.8
2009	250	70.7	52.3	212.7	29.9	46.8	72.3
2009	262	22.4	58.7	50.1	−25.9	−140.5	−56.7
2009	274	79.4	82.3	287.7	−64.9	−28.9	−26.4
2009	281	75.5	75.3	256.7	14.0	34.2	29.4
2009	282	47.2	60.8	47.6	11.5	168.6	−38.7
2009	288	34.2	58.6	217.9	−51.5	−41.6	8.4

Table 2—Continued

Year	Julian day	θ [°]	E [EeV]	α [°]	δ [°]	ℓ [°]	b [°]
2009	304	30.1	55.6	177.7	−5.0	−83.8	54.7
2009	335	64.2	52.5	171.3	−43.8	−73.1	16.4
2010	24	73.6	54.3	97.2	34.3	179.7	10.6
2010	45	70.0	61.5	174.7	−21.2	−78.9	38.6
2010	50	71.7	64.5	227.9	−21.5	−18.6	30.7
2010	52	52.1	72.9	258.1	−44.9	−17.0	−3.3
2010	72	43.3	66.9	278.8	7.9	38.2	7.2
2010	121	43.6	82.0	122.7	−70.7	−76.3	−19.3
2010	148	52.2	74.8	89.2	−12.0	−142.2	−17.5
2010	182	15.4	54.7	197.8	−20.0	−50.7	42.6
2010	193	69.6	58.4	149.2	5.5	−127.5	43.2
2010	194	70.9	53.8	277.2	6.7	36.4	8.1
2010	196	73.2	52.3	303.7	−68.1	−32.6	−32.8
2010	204	38.7	53.2	180.5	−11.5	−75.9	49.6
2010	205	47.4	53.5	315.8	−82.1	−49.3	−31.2
2010	223	39.0	56.1	250.2	−73.6	−42.6	−17.5
2010	224	62.3	65.2	284.7	−28.2	8.1	−13.9
2010	226	53.8	75.6	324.5	17.9	71.2	−25.0
2010	235	32.0	60.3	216.1	−66.5	−48.0	−5.3
2010	238	12.4	69.6	226.4	−25.7	−22.6	28.1
2010	239	66.7	58.4	312.9	−14.2	33.1	−33.0
2010	256	73.8	76.1	131.9	−15.5	−118.9	17.1
2010	277	31.1	73.7	12.3	−40.7	−55.3	−76.5
2010	284	48.6	89.1	218.8	−70.8	−48.7	−9.7
2010	295	27.8	58.0	8.4	−61.5	−53.3	−55.5
2010	310	45.4	53.1	118.1	8.5	−147.9	17.4
2010	311	58.4	70.5	64.2	−46.5	−107.2	−45.5
2010	319	11.4	55.0	118.6	−37.4	−107.2	−4.8
2010	320	29.0	54.3	80.2	−64.1	−86.2	−34.1
2010	320	5.1	68.7	121.1	−30.6	−111.9	0.4
2010	342	40.5	54.6	170.9	−43.7	−73.4	16.4
2010	347	24.6	54.9	231.9	−56.6	−36.7	0.0
2010	348	33.8	54.4	179.7	−68.6	−61.9	−6.2
2010	364	22.2	68.0	167.0	−31.2	−81.8	26.6
2011	19	43.8	69.4	268.5	−15.7	12.4	5.1
2011	26	25.0	100.1	150.1	−10.3	−110.9	34.1
2011	35	71.5	54.0	185.4	−24.6	−65.6	37.8
2011	38	33.8	58.2	33.4	−31.7	−127.8	−71.5

Table 2—Continued

Year	Julian day	θ [°]	E [EeV]	α [°]	δ [°]	ℓ [°]	b [°]
2011	41	59.2	52.0	125.5	−59.2	−86.0	−12.5
2011	45	25.5	62.7	215.5	−10.1	−23.5	46.8
2011	49	39.3	60.3	239.4	3.9	13.8	39.9
2011	75	60.5	71.1	230.3	1.5	3.8	45.9
2011	86	59.4	56.2	160.3	−3.1	−108.3	46.4
2011	106	78.2	81.4	308.8	16.1	59.9	−14.3
2011	111	65.6	69.7	30.3	3.8	154.2	−54.8
2011	113	71.5	54.8	295.1	−27.6	12.2	−22.3
2011	119	53.0	67.3	255.4	−5.1	14.8	21.6
2011	120	49.8	72.1	84.9	14.4	−168.3	−8.7
2011	132	10.6	56.8	39.5	−29.9	−134.1	−66.5
2011	136	54.1	64.9	333.8	−79.2	−48.7	−35.3
2011	162	72.4	55.9	132.8	12.9	−145.5	32.4
2011	203	29.9	77.9	120.8	−56.3	−89.8	−13.2
2011	207	65.0	56.4	344.5	−19.9	42.3	−63.1
2011	215	34.5	68.3	245.4	−18.2	−2.8	21.8
2011	221	2.9	70.8	139.8	−35.8	−98.2	9.6
2011	240	46.5	58.8	219.1	−41.9	−36.9	16.8
2011	252	24.5	80.9	283.7	−28.6	7.4	−13.2
2011	294	31.8	75.6	77.2	−41.0	−114.4	−36.1
2011	307	40.7	52.4	313.5	−16.6	30.7	−34.4
2011	309	38.8	63.3	26.1	−32.2	−120.2	−77.4
2011	316	31.0	70.2	4.6	−37.9	−26.2	−77.2
2011	318	36.7	57.2	148.8	−13.0	−109.6	31.4
2011	360	36.1	67.4	305.5	−34.5	7.6	−32.7
2011	361	47.6	92.8	343.4	−71.6	−44.9	−42.6
2011	364	51.7	64.8	207.1	−29.1	−42.4	32.1
2012	12	31.8	62.4	15.3	−3.6	129.0	−66.3
2012	52	23.8	66.1	33.2	−59.0	−75.3	−55.2
2012	81	47.3	99.0	309.4	−66.8	−31.5	−35.2
2012	103	67.5	70.4	154.0	−46.3	−83.1	8.6
2012	109	25.9	62.6	37.8	−39.5	−110.0	−65.9
2012	132	62.3	58.5	189.0	−5.1	−64.1	57.6
2012	154	65.8	58.7	37.0	−75.8	−64.6	−39.9
2012	155	64.3	60.0	245.4	−30.9	−12.7	13.3
2012	162	58.5	83.8	26.8	−24.8	−154.6	−77.3
2012	183	59.8	61.8	259.8	−32.7	−6.2	2.7
2012	189	31.4	61.1	18.7	−42.5	−72.9	−73.9

Table 2—Continued

Year	Julian day	θ [°]	E [EeV]	α [°]	δ [°]	ℓ [°]	b [°]
2012	193	65.5	54.4	342.9	−6.5	63.4	−54.8
2012	206	61.6	56.8	310.6	−83.1	−50.0	−30.2
2012	211	50.0	58.7	177.2	12.5	−105.1	69.3
2012	301	38.5	53.3	56.3	−3.2	−169.2	−42.1
2012	332	48.1	71.1	227.6	11.9	14.7	54.0
2013	11	17.0	55.7	217.1	−24.5	−30.5	33.3
2013	27	26.5	62.7	200.9	−34.6	−49.6	27.8
2013	27	47.6	70.7	56.6	−67.8	−77.6	−41.7
2013	31	67.3	53.2	314.9	−67.3	−32.8	−37.1
2013	36	74.7	73.6	267.5	−68.3	−34.8	−19.7
2013	52	60.7	71.9	73.7	−20.5	−139.8	−34.4
2013	70	41.9	53.9	154.3	−15.8	−102.7	33.1
2013	119	61.5	62.1	138.6	26.1	−158.8	41.9
2013	132	59.3	57.3	357.0	−81.1	−54.1	−35.7
2013	134	44.9	85.3	123.4	−6.2	−131.7	15.1
2013	144	49.8	54.3	33.3	−39.0	−107.2	−69.2
2013	163	44.6	52.2	0.4	−68.1	−50.1	−48.3
2013	175	50.6	58.9	211.1	15.0	1.0	69.1
2013	190	57.3	68.8	64.7	−70.1	−77.0	−38.0
2013	191	8.8	67.3	308.1	−39.5	2.1	−35.7
2013	222	63.4	61.5	240.3	−68.9	−41.3	−12.1
2013	224	47.9	63.4	345.4	−9.0	62.7	−58.3
2013	247	54.7	84.8	154.6	−46.9	−82.4	8.3
2013	249	30.0	55.5	160.4	−34.8	−85.2	20.9
2013	249	55.0	65.4	92.1	−64.1	−86.4	−28.9
2013	281	65.1	58.5	327.5	−25.1	25.3	−49.4
2013	297	39.0	73.0	163.8	−74.1	−64.9	−13.1
2013	302	49.4	54.6	298.7	8.8	48.2	−9.8
2013	319	62.0	54.4	284.5	−37.6	−1.0	−17.3
2013	320	22.2	52.9	286.8	−55.0	−18.3	−24.1
2013	329	29.2	63.6	182.3	−14.3	−72.3	47.3
2013	332	31.1	65.2	241.6	−53.5	−30.5	−1.0
2013	352	51.4	72.5	91.4	−60.6	−90.4	−28.9
2013	364	60.2	53.2	198.8	−63.9	−54.5	−1.2
2014	8	57.9	60.0	72.8	−73.5	−74.4	−34.3
2014	30	60.8	74.5	189.9	−32.7	−60.0	30.1
2014	32	12.8	54.6	186.7	−24.9	−64.1	37.6
2014	49	41.7	54.9	2.3	−49.2	−39.7	−66.4

Table 2—Continued

Year	Julian day	θ [°]	E [EeV]	α [°]	δ [°]	ℓ [°]	b [°]
2014	59	25.9	60.2	239.5	-49.2	-28.7	3.0
2014	64	66.7	63.6	45.2	-65.8	-75.6	-46.4
2014	65	58.5	118.3	340.6	12.0	80.1	-39.9